OCEAN
ISSN 3008-1203
Open Access
Research Article

Effect of flow incidence angle on vortex-induced motion of a semi-submersible floating offshore wind turbine platform

Xianghan Yin[1], Enhao Wang[1] ✉, Hongteng Xu[1], Hao Wu[1], Yuanchuan Liu[2], Binbin Li[1] ✉, Lin Lin[3], Qing Xiao[4], and Atilla Incecik[4]

[1] Institute for Ocean Engineering, Shenzhen International Graduate School, Tsinghua University, Shenzhen 518055, China
[2] College of Engineering, Ocean University of China, Qingdao 266404, China
[3] SGIDI Engineering Consulting (Group) Co., Ltd., Shanghai 200093, China
[4] Department of Naval Architecture, Ocean and Marine Engineering, University of Strathclyde, Glasgow G4 0LZ, UK

Cite This: *Ocean*, **2025**, *1*, 9470003

Read Online

ABSTRACT: A computational fluid dynamics study is conducted to investigate the effect of the flow incidence angle (θ) on the three-degree-of-freedom vortex-induced motion (VIM) of a DeepCWind semi-submersible floating offshore wind turbine platform. A scaled model with a scaling factor of 1:72.72 and three θ values, i.e., θ = 0°, 90°, and 180° are considered. The reduced velocity (V_R) is varied from 3 to 15. The response characteristics, hydrodynamic coefficients, motion trajectories, and wake patterns are analysed in detail. Substantial cross-flow VIM is observed in the V_R range of 6–10 while distinct vortex-induced yaw motion appears at higher V_R. Under the diverse effects of the vortex shedding modes at different θ values, the motion trajectories of the platform exhibit figure-eight and raindrop shapes. When θ = 90° and 180°, the wake of the upstream side columns influences the vortex shedding of the downstream side columns, disrupting the vortex field and subsequently suppressing the VIM. In addition, the smaller structural members, namely the pontoons and the cross braces also impose a damping effect on the VIM. The pontoons interfere with the vortices from the upstream side columns at the lower part of the platform and two symmetric vortex streets are formed behind the cross braces inducing a restoring moment against the yaw motion.

KEYWORDS: floating offshore wind turbine, semi-submersible platform, vortex-induced motion, large eddy simulation , flow incidence angle

1 Introduction

In recent years, offshore wind energy has emerged as a highly promising form of renewable energy, demonstrating remarkable growth since 2015. The share of offshore wind energy in the global wind energy market has experienced a significant increase escalating from 4.55% to 6.71% between 2019 and 2021 with the total capacity surging from 28.3 to 55.7 GW [1]. The focus of wind energy exploitation is progressively shifting towards offshore regions because of the ample wind energy resources in the deep-sea areas [2]. In this context, the deployment of floating offshore wind turbines (FOWTs) has become an economically viable and practical solution [3].

A FOWT comprises three primary components: the wind turbine, the floating platform, and the mooring system. Among these elements, the platform encounters the most intricate loading conditions. The combined influence of wind, waves, and currents induces the six-degree-of-freedom (6DOF) motion of the platform, leading to the unsteady power output of the turbine [4]. Consequently, a thorough investigation into the dynamic characteristics of the platform becomes imperative for the design of the FOWT. In contrast to the spar and tension leg platform (TLP), the semi-submersible floater offers enhanced cost effectiveness and demonstrates a more stable hydrodynamic behaviour, which renders it particularly favourable for the engineering applications and emphasises its significance as a crucial area of research [5].

Currently, investigations into the FOWT semi-submersible platforms are predominantly focused on exploring the dynamic responses caused by wind and waves [6,7]. However, a significant gap exists in understanding the influence of ocean currents. Insights gleaned from the extensive studies on similar semi-submersible platforms in the oil and gas industry reveal that periodic vortex shedding causes substantial motion responses in both the in-line and cross-flow directions when the platforms are exposed to ocean currents [8,9]. This phenomenon, known as the vortex-induced motion (VIM), manifests as a special form of vortex-induced vibration (VIV) at high Reynolds numbers ($Re = UD/\nu$, where U is the freestream velocity, D is the characteristic length of the structure, and ν is the kinematic viscosity of the fluid), small aspect ratios, low mass ratios, and multiple degrees of freedom [10]. These characteristics are also applicable to the FOWT semi-submersible platforms. The VIM behaviour significantly amplifies the fatigue

Received: July 23, 2024; **Revised:** August 20, 2024
Accepted: September 20, 2024

✉Address correspondence to Enhao Wang, enhao.wang@sz.tsinghua.edu.cn; Binbin Li, libinbin@sz.tsinghua.edu.cn

and extreme responses of the FOWTs, increasing the low-frequency tension in the mooring system and adversely affecting the power generation stability of the wind turbine [11]. However, there are currently no specific analytical design methods outlined in the relevant international rules, regulations, and standards. Instead, there is a greater reliance on the empirical models and experimental tests.

Numerous scaled model tests have been conducted for various semi-submersible platforms to unveil their VIM characteristics subject to current loads. For different flow incidence angle (θ) values, Rijken et al. [9] reported notable variations in the response amplitudes in both the in-line and cross-flow directions with evident occurrences of the lock in over certain velocity ranges. In the experimental tests of Hussain et al. [12], it was discovered that the yaw motion was dramatic at an incidence angle of $\theta = 0°$. Liu et al. [13] confirmed that θ played a vital role in affecting the in-line and cross-flow VIM responses of the semi-submersible platform. In addition to the flow conditions, the intrinsic properties of the platform also influence its VIM behaviours. In the study of Waals et al. [8], model tests were performed on four distinct semi-submersible platforms featured by a configuration of four squared columns. The platforms with lower mass ratios and deeper drafts exhibited augmented responses. Gonçalves et al. [14] examined the impact of different column shapes on the VIM responses of deep-draft semi-submersible platforms and significant variations were noticed. Their subsequent experiments [15] demonstrated that circular columns elicited larger cross-flow VIM amplitudes compared with squared ones. Moreover, different roughness levels influenced the shedding of wake vortices, leading to the disparities in the VIM responses. Further analysis through model tests of three-column FOWT semi-submersible platforms incorporating three distinct column geometries (i.e., circular, squared, and diamond) confirmed the superior in-line and cross-flow VIM of the platform with circular columns at $\theta = 0°$ [16]. In addition, pontoons were identified to exert a suppressive effect on the VIM responses across various configurations [17]. A comparative evaluation between a semi-submersible platform equipped with four circular columns with pontoons and the same one without pontoons showed alleviated cross-flow VIM amplitude in the former configuration [18]. Although model tests are considered to be relatively accurate, challenges such as the scaling effects and the limitations of the experimental conditions persist. Moreover, strict adherence to the similarity criteria can introduce unphysical representation of certain quantities. Rijken et al. [19] observed that the response amplitudes of the semi-submersible platforms obtained from the model tests tended to surpass the field measurement data. These discrepancies stem from the considerable constraints imposed by the actual experimental conditions. Wu et al. [20] also identified significant differences between the model test outcomes and field measurements for a four-column semi-submersible platform, whereas the results from the computational fluid dynamics (CFD) simulations conducted at various scales were in better agreement with their experimental counterparts.

With the advancement of CFD, there has been a growing trend in its application to the prediction of the VIM of FOWT platforms as well as the assessment of the scaling effects and the evaluation of innovative approaches to mitigate VIM. For instance, numerical simulations were employed to explore the combined effects of the wind and wave loads on the motion responses [21–23]. Liu et al. [24] and Liu et al. [25] conducted simulations of the DeepCWind FOWT semi-submersible platform across a wide range of current velocities. They found that specific θ values and column configurations could lead to maximised VIM, which was consistent with the findings from the model tests [26]. The results also revealed the complicated interactions between the vortices and the platform during the VIM, whereas the base columns exhibited a damping effect on the transverse response of the floater. Further research on this FOWT platform with different θ values indicated the occurrences of the VIM under diverse operational scenarios [27]. However, it should be noted that only two translational degrees of freedom were considered in these studies and the geometry of the platform was simplified, which potentially overlooked the significant influence of pontoons and cross braces on the VIM responses as evidenced by Tian et al. [28] and Gonçalves et al. [29]. Therefore, it is necessary to investigate the effects of those structural members on the VIM of the FOWT semi-submersible platform. In addition, the vortex-induced yaw motion which has not been properly addressed in the previous studies should also be analysed, given its potential to cause unbalanced loads on the semi-submersible platforms as suggested in Ref. [30]. A critical aspect of the CFD simulations in the context of the VIM of the semi-submersible FOWT platforms lies in the selection of an appropriate turbulence model. Commonly used turbulence models encompass Reynolds-averaged Navier–Stokes (RANS) equations, detached eddy simulation (DES), and large eddy simulation (LES). Kim et al. [31] adopted delayed DES and unsteady RANS to study the VIM of an octagonal column semi-submersible platform. The results indicated that DES effectively captured the intricate vortex structures and yielded VIM responses aligning more closely with the experimental data. Liu et al. [25] and Liu et al. [27] utilised unsteady RANS and DES to examine the two-DOF (2DOF) VIM of the DeepCWind semi-submersible platform and also manifested the ability of DES to depict more refined characteristics in the vortex field than the RANS model. Compared to the RANS and DES approaches, the LES method is more accurate in reproducing the vortex structures in turbulent flow and it has been proven that the LES method is capable of simulating the complex VIV and VIM phenomena [32–35]. However, the application of LES in the simulations of the VIM of FOWT platforms is still quite limited, which requires further investigation.

In this study, CFD simulation of the VIM of the DeepCWind semi-submersible platform is conducted to investigate the effect of θ on the motion responses, hydrodynamic characteristics, three-dimensional (3D) wake structures, and vortex shedding modes. This semi-submersible floater was originally designed to support National Renewable Energy Laboratory (NREL) offshore 5 MW baseline turbine and was defined in the OC4 project Phase II. It consists of a main column (MC) and three side columns interconnected by cross braces and pontoons as shown in Fig. 1a [36]. The influence of the cross braces and pontoons is taken into account and the platform undergoes three-DOF (3DOF) VIM (i.e., in-line, surge and cross-flow, and sway and yaw) in the present simulation. The outline of the rest of the paper is as follows. The numerical method and the computational model utilised in the simulation are introduced in Section 2. Detailed geometry of the platform and the simulation parameters are provided in Section 3. In Section 4, the results are presented and analysed comprehensively. Finally, the main conclusions of this paper are summarised in Section 5.

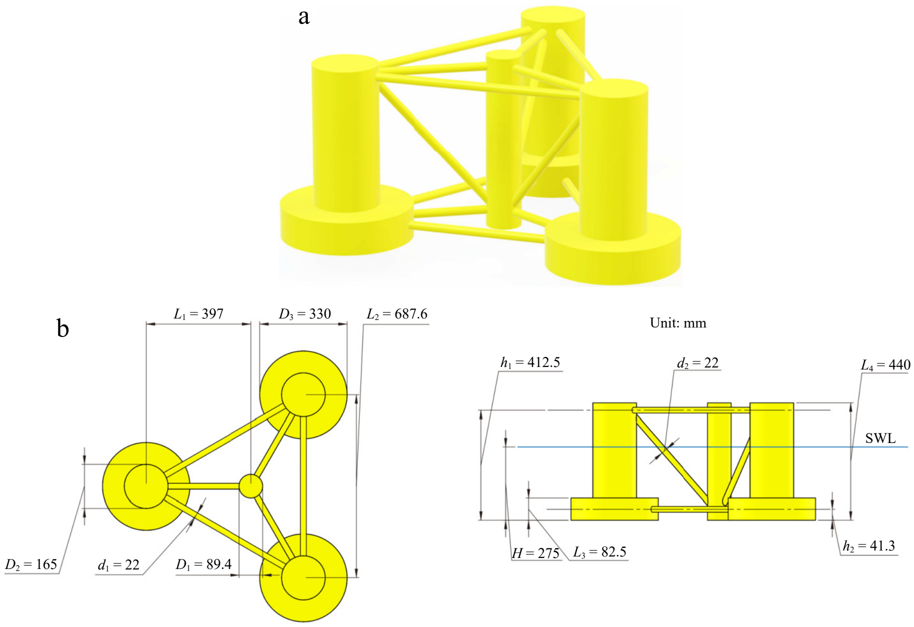

Figure 1 Geometry definition of the DeepCWind semi-submersible platform. 3D overview (a) and etailed dimensions (b) of the scaled model (SWL: still water level).

2 Numerical method

2.1 Flow model

The flow around the DeepCWind semi-submersible platform is modelled by solving the unsteady incompressible Navier–Stokes equations. The LES wall-adapted local eddy-viscosity (WALE) model [37] is utilised for turbulence modelling. The LES WALE model is advantageous because of its capabilities of reproducing the laminar to turbulent transition and returning the correct wall-asymptotic (y^{+3}) variation of the subgrid-scale (SGS) viscosity.

The arbitrary Lagrangian–Eulerian (ALE) scheme [38] is employed to deal with the moving boundary and the dynamic mesh problems. The ALE form of the governing equations in the Cartesian coordinate system can be expressed as follows

$$\frac{\partial \bar{u}_i}{\partial x_i} = 0 \tag{1}$$

$$\frac{\partial \bar{u}_i}{\partial t} + (\bar{u}_j - \widehat{u}_j)\frac{\partial \bar{u}_i}{\partial x_j} = -\frac{1}{\rho}\frac{\partial \bar{p}}{\partial x_i} + \nu \nabla^2 \bar{u}_i - \frac{\partial \tau_{ij}^S}{\partial x_j} \tag{2}$$

where $(x_1, x_2, x_3) = (x, y, z)$ represent the Cartesian coordinates, an overbar stands for a filtered variable, $\bar{u}_i$ and $\widehat{u}_j$ are the flow velocity component and the grid velocity component in the x_i direction, respectively, t is the time, ρ represents the fluid density, and p denotes the pressure. Equations (1) and (2) describe the temporal and spatial evolution of the large and energy carrying scales of motion. The nonlinearity of the convective term leads to the appearance of the so-called SGS stress tensor.

$$\tau_{ij}^S = |\overline{u_i u_j}| - \bar{u}_i \bar{u}_j \tag{3}$$

which accounts for the effects of the unresolved scales. The eddy-viscosity models relate the SGS stresses to the large-scale strain-rate tensor ($\bar{S}_{ij}$) as follows

$$\tau_{ij}^S - \frac{\delta_{ij}}{3}\tau_{kk}^S = -2\nu_{\mathrm{T}}\bar{S}_{ij} \tag{4}$$

where δ_{ij} is the Kronecker symbol, and ν_{T} is eddy viscosity. The isotropic part of the SGS stresses (τ_{kk}^S) is added to the filtered pressure. $\bar{S}_{ij}$ denoting the resolved scale can be defined by

$$\bar{S}_{ij} = \frac{1}{2}\left(\frac{\partial \bar{u}_i}{\partial x_j} + \frac{\partial \bar{u}_j}{\partial x_i}\right) \tag{5}$$

The ν_{T} is computed by

$$\nu_{\mathrm{T}} = (C_{\mathrm{w}}\Delta)^2 \frac{\left(S_{ij}^d S_{ij}^d\right)^{3/2}}{\left(\bar{S}_{ij}\bar{S}_{ij}\right)^{5/2}\left(S_{ij}^d S_{ij}^d\right)^{5/4}} \tag{6}$$

where the model constant (C_{w}) = 0.325. The width of the filter is taken as the local grid size, i.e., $\Delta = \sqrt[3]{\Delta x \Delta y \Delta z}$ with Δx, Δy, and Δz, and being the local grid size in the x, y, and z direction, respectively. S_{ij}^d stands for the traceless symmetric part of the square of the velocity gradient tensor.

$$S_{ij}^d = \frac{1}{2}\left(\bar{g}_{ij}^2 + \bar{g}_{ji}^2\right) - \frac{1}{3}\delta_{ij}\bar{g}_{kk}^2 \tag{7}$$

where $\bar{g}_{ij}^2 = \bar{g}_{ik}\bar{g}_{kj}$ and $\bar{g}_{ij} = \partial \bar{u}_i / \partial x_j$. The tensor S_{ij}^d can be expressed in terms of the strain-rate and the vorticity tensors.

$$S_{ij}^d = \bar{S}_{ik}\bar{S}_{kj} + \bar{\Omega}_{ik}\bar{\Omega}_{kj} - \frac{1}{3}\delta_{ij}\left(\bar{S}_{mn}\bar{S}_{mn} + \bar{\Omega}_{mn}\bar{\Omega}_{mn}\right) \tag{8}$$

here, the vorticity tensor is given by

$$\bar{\Omega}_{ij} = \frac{1}{2}\left(\frac{\partial \bar{u}_i}{\partial x_j} - \frac{\partial \bar{u}_j}{\partial x_i}\right) \tag{9}$$

The flow field is simulated with the open source CFD toolbox OpenFOAM (ESI version v2106). A finite volume method (FVM) is adopted for the discretisation of the governing equations. The transient term is discretised with a second-order implicit backward scheme. A second-order Gauss linear scheme is employed to discretise the gradient terms. A linear upwind stabilised transport (LUST) scheme with second-order accuracy is used as the convection scheme. A Gauss linear corrected scheme is utilised for the discretisation of the diffusion terms. The pressure–velocity coupling is solved by the pressure-implicit with splitting of operators (PISO) algorithm [39] in a segregated manner.

2.2 Structural dynamic model

The moored semi-submersible platform essentially constitutes an elastically supported system. In this study, the floater is free to move in 3DOFs, namely in-line, cross-flow, and yaw. The corresponding equations of motion are as follows

$$m_x\ddot{x}(t)+c_x\dot{x}(t)+k_x x(t)=F_x(t) \tag{10}$$

$$m_y\ddot{y}(t)+c_x\dot{y}(t)+k_y y(t)=F_y(t) \tag{11}$$

$$I_\alpha\ddot{\alpha}(t)+c_\alpha\dot{\alpha}(t)+k_\alpha \alpha(t)=M(t) \tag{12}$$

where $m_x = m_y = m$ denotes the mass of the floater, I_α is the moment of inertia about the yaw axis, c_x, c_y, and c_α are the structural damping coefficients, and k_x, k_y, and k_α stand for the structural stiffness in the in-line, cross-flow, and yaw directions, respectively, x, y and α are the in-line displacement, cross-flow displacement, and the yaw angle, respectively, a dot represents differentiation with respect to time, double dot is the second derivative with respect to time, F_x and F_y are the hydrodynamic forces in the in-line and cross-flow directions, and M stands for the moment about the yaw axis. The implicit Newmark-β method with second-order accuracy as detailed in Ref. [40] is employed to numerically integrate the three preceding equations. In the present research, the two real parameters (β and γ) concerning the accuracy and stability are selected as β = 1/4 and γ = 1/2, corresponding to the average acceleration method with unconditional stability.

2.3 Fluid–structure interaction (FSI)

The FSI problem in this study is modelled in a loosely coupled manner. The information is only exchanged once per time step between the flow model and the structural dynamic model without any sub-iterations. At the beginning of the simulation, the flow field around the platform is initialised. Within each time step, the hydrodynamic forces are computed by integrating the pressure and the viscous shear stress over the surface of the platform Γ as $\int_\Gamma \left\{-p\boldsymbol{I}+\mu\left[\nabla\boldsymbol{u}+(\nabla\boldsymbol{u})^{\mathrm{T}}\right]\right\}\cdot n\mathrm{d}\Gamma$, where $\boldsymbol{I}$ represents the unit tensor, μ stands for the dynamic viscosity of the fluid, $\boldsymbol{u}$ is the flow velocity vector, and $\boldsymbol{n}$ is the outward pointing vector normal to the surface of the platform. Then, by solving Eqs. (10)–(12), the motion quantities of the platform are derived. After that, the spherical linear interpolation (SLERP) of the motion quantities as a function of the distance to the platform surface is performed to obtain the new mesh positions and velocities. The SLERP interpolation method enforces smoothness, and the distance function has a cosine profile to preserve shape of cells close to the moving surface. Subsequently, the mesh is morphed based on the updated velocity boundary conditions of the platform, and the next time step begins with solving the governing equations in Section 2.1 on the updated mesh. This FSI loop is repeated in each time step until the end of the simulation.

3 Problem description

3.1 Simulation parameters

In order to facilitate the comparison, the DeepCWind semi-submersible model with a scaling factor of 1:72.72 as in Gonçalves et al. [26] is used in the present study. Figures 1b and 1c show the main dimensions of the platform with their specific values tabulated in Table 1. Similar to the setup in the experimental tests [26] and the numerical study of Rentschler et al. [41], four springs are attached to the floater via a rigid plate on top of the platform to serve as the mooring lines. This plate is not modelled in the simulation but the attachment points (the fairleads) on it, as well as its mechanical properties are considered in the structural dynamic solver. When the platform is in its equilibrium position, the two springs attached to the anchors and the platform in the x = 0 plane are referred to as the front and back springs and the other two springs in the y = 0 plane are referred to as the left and right springs. Detailed parameters of the mooring lines are tabulated in Table 2. As discussed by Gonçalves et al. [26], the structural damping ratio for the experimental tests is ζ_s = 0.1%, which is almost negligible. Therefore, the damping of the mooring lines is set to zero in this study. It should also be noted that the anchor and the fairlead coordinates in the present research are slightly different from those adopted by Rentschler et al. [41] as the centre of gravity (COG) of the platform is modified to coincide with the origin of the Cartesian coordinate system. The inertial properties of the scaled model are summarised in Table 3.

In the present simulation, the platform is free to respond in 3DOFs, i.e., in-line (surge), cross-flow (sway), and yaw. Three θ values of θ = 0°, 90°, and 180° are considered as depicted in Fig. 2. For each θ value, the reduced velocity ($V_{\mathrm{R}} = UT_{\mathrm{ny}}/D$, where T_{ny} denotes the natural period of the platform in the transverse direction in still water) is varied from 3 to 15 with an increment of 1, and the corresponding U and Re are listed in Table 4. Due to the fact that the T_{ny} value of θ = 90° is distinct from that of θ = 0° and 180°, for a certain V_{R} value, U and Re are different when θ = 0° and 180° and θ = 90°, respectively.

Table 1 Main dimensions of the scaled DeepCWind FOWT platform model

Dimension	Value (mm)
Draft, H	275.0
Distance between the main and side columns, L_1	397.0
Distance between the side columns, L_2	687.6
Height of the side column base, L_3	82.5
Total height of the side column, L_4	440.0
Diameter of the MC, D_1	89.4
Diameter of the upper part of side columns, D_2	165.0
Diameter of the side column base, D_3	330.0
Diameter of the pontoons, d_1	22.0
Diameter of the cross braces, d_2	22.0
Height between the upper pontoons and platform base, h_1	412.5
Height between the lower pontoons and platform base, h_2	41.3

Table 2 Mooring line parameters under equilibrium conditions

Spring	Anchor coordinate (m)	Fairlead coordinate (m)	Stiffness (N/m)	Damping (Ns/m)	Unstretched length (m)
Front	(2.4, 0, 0.346)	(0.49, 0, 0.141)	7.4556	0	0.800
Back	(−2.4, 0, 0.346)	(−0.49, 0, 0.141)	7.4556	0	0.800
Left	(0, −0.159, 0.346)	(0, −0.49, 0.141)	9.4176	0	0.425
Right	(0, 0.159, 0.346)	(0, 0.49, 0.141)	9.4176	0	0.425

https://doi.org/10.26599/OCEAN.2025.9470003

Table 3 Inertial properties of the scaled DeepCwind FOWT platform model

Parameter	Value
Mass of the platform model, m	36.70 kg
Height of centre of mass below SWL, H_{CM}	141.00 mm
Radius of gyration, R_{zz}	330.00 mm

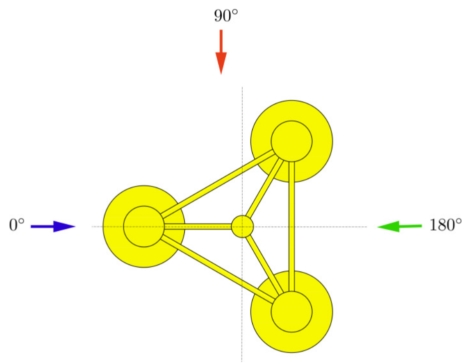

Figure 2 Three θ for the DeepCWind FOWT platform model in the present simulation.

Table 4 Freestream velocities and Re in the present simulation

V_R	U (m/s)		Re	
	0° and 180°	90°	0° and 180°	90°
3	0.0516	0.0510	8.51×10^3	8.42×10^3
4	0.0688	0.0680	1.13×10^4	1.12×10^4
5	0.0859	0.0851	1.42×10^4	1.40×10^4
6	0.1031	0.1021	1.70×10^4	1.68×10^4
7	0.1203	0.1191	1.99×10^4	1.96×10^4
8	0.1375	0.1361	2.27×10^4	2.25×10^4
9	0.1547	0.1531	2.55×10^4	2.53×10^4
10	0.1719	0.1701	2.84×10^4	2.81×10^4
11	0.1891	0.1871	3.12×10^4	3.09×10^4
12	0.2063	0.2041	3.40×10^4	3.37×10^4
13	0.2234	0.2211	3.69×10^4	3.65×10^4
14	0.2406	0.2381	3.97×10^4	3.93×10^4
15	0.2578	0.2552	4.25×10^4	4.21×10^4

3.2 Computational domain and boundary conditions

The computational domain for the simulation is shown in Fig. 3 with the case of θ = 0° selected for demonstration. The size of the computational domain is $60D \times 40D \times 9.6H$. The COG of the platform is located $20D$ downstream the inlet boundary, $40D$ upstream the outlet boundary, and $20D$ away from the two lateral boundaries. The platform is rotated about the z axis to take into account the different θ values. The following boundary conditions are adopted: At the inlet boundary, a constant flow velocity $\boldsymbol{U} = (U, 0, 0)$ is utilised with the gradient of the pressure in the direction normal to the boundary being $\partial p/\partial \boldsymbol{n} = 0$, a zero gradient boundary condition is employed for the velocity ($\partial \boldsymbol{U}/\partial \boldsymbol{n} = 0$) on the outlet boundary, and a zero reference pressure ($p_{\mathrm{ref}} = 0$) is prescribed, and a symmetry boundary condition is applied to the rest of the four boundaries of the computational domain. The surface of the platform is assumed to be smooth with a no-slip boundary condition ($\boldsymbol{U} = \boldsymbol{U}_s$, where $\boldsymbol{U}_s$ is the velocity of the platform) being implemented.

The background mesh of the computational domain is generated using the blockMesh utility of OpenFOAM with a grid size of 0.1 m. Then, the snappyHexMesh utility is adopted to iteratively refine and snap the mesh to the platform surface. A total of 15 prismatic cell layers with the first layer height of 3×10^{-5} m and an expansion ratio of 1.2 are extruded from the platform surface to ensure that the y^+ value is less than 1 in order to capture the boundary layer separation and the vortex structures more accurately.

The computational mesh for θ = 0° is displayed in Fig. 4. The total number of cells is 4.24 million. As shown in Fig. 4a, three refinement regions are added around the platform and in the wake to progressively refine the mesh. Figure 4b further demonstrates two more mesh refinements approaching the MC and the cross braces as well as the details of the prism layers via a close up of the mesh around those structural members. From the overall 3D grid as illustrated in Fig. 4c, the isotropic grid refinement is observed by the cutting planes normal to the y and z directions.

3.3 Mesh dependency study

To evaluate the effect of the mesh density on the numerical results, a mesh dependency study on the 3DOF VIM of the DeepCWind platform at θ = 0° and V_R = 8 is performed using three different meshes. The comparison of the results from the three different meshes is presented in Table 5, where N_c is the number of cells, $\bar{x}/D$ stands for the nondimensional mean in-line displacement, A_x/D, A_y/D, and A_α are respectively the dimensionless amplitudes of the in-line, cross-flow, and yaw responses, $\bar{C}_D$, C_D', and C_L' denote the mean drag coefficient, the root mean square (rms) value of the fluctuating drag coefficient, and the rms value of the fluctuating lift coefficient, respectively. The drag and lift coefficients are computed by

$$C_D = \frac{F_D(t)}{\frac{1}{2}\rho A_p U^2} \tag{13}$$

$$C_L = \frac{F_L(t)}{\frac{1}{2}\rho A_p U^2} \tag{14}$$

herein, $A_p = 3 \times [D_2(H - L_3) + D_3L_3]$ and the nondimensional response amplitudes are defined as

$$A_x/D = \sqrt{2}x_{\mathrm{rms}}/D \tag{15}$$

$$A_y/D = \sqrt{2}y_{\mathrm{rms}}/D \tag{16}$$

$$A_\alpha = \sqrt{2}\alpha_{\mathrm{rms}} \tag{17}$$

where x_{rms}, y_{rms}, and α_{rms} represent the root mean square values of the steady-state in-line, cross-flow, and yaw motion responses. It can be interpreted from Table 5 that the maximum deviation of 18.4% between the results of M1 and M2 is observed in C_L', whereas the maximum difference between the results of M2 and M3 reduces to approximately 6.41%. Given the variation in the performances of the LES model for different mesh densities, the comparison suggests that the results from M2 are deemed acceptable, and mesh density similar to that of M2 is used in the numerical simulation in this paper balancing the accuracy and computational efforts.

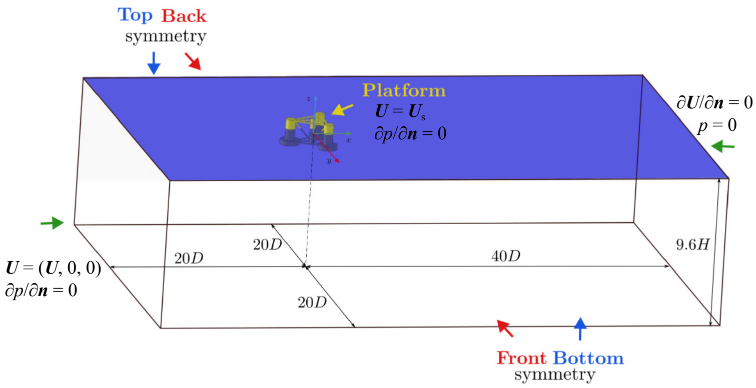

Figure 3 Computational domain and boundary conditions.

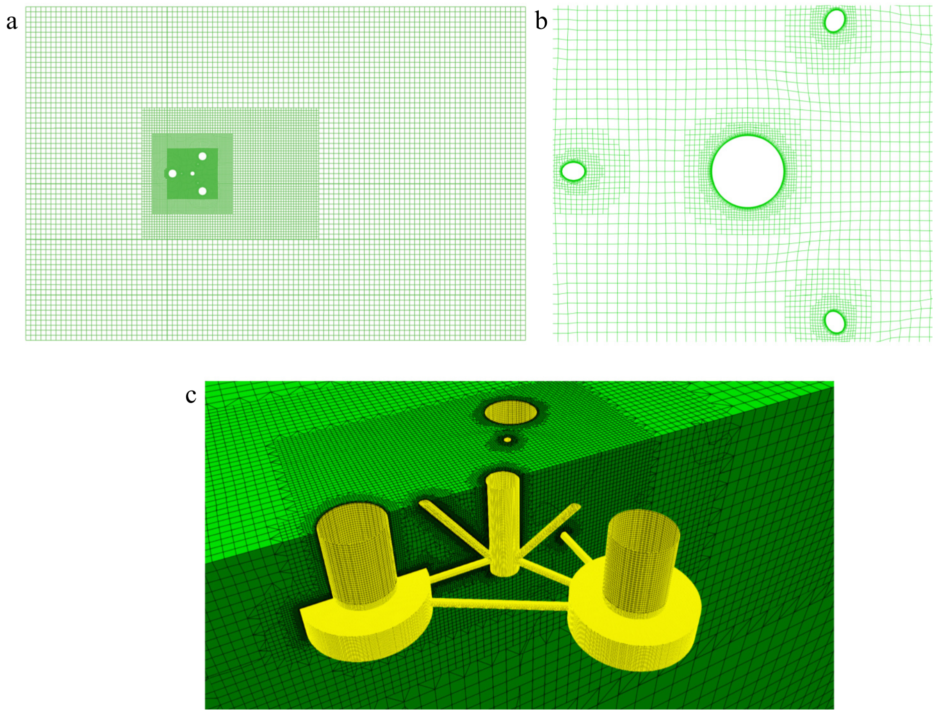

Figure 4 Computational mesh. (a) Slice normal to the *xy* plane. (b) A close up of the mesh near the MC and the cross braces. (c) 3D view of the grid around the platform.

Table 5 Comparison of the results from different meshes

Mesh	N_c	$\bar{x}/D$	A_x/D	A_y/D	A_α	$\bar{C}_D$	C'_D	C'_L
M1	2,742,223	0.4505	0.0402	0.5139	0.5537	1.1718	0.0867	0.2939
M2	4,243,867	0.4410	0.0473	0.5138	0.4916	1.1556	0.0877	0.3603
M3	5,977,845	0.4497	0.0463	0.5332	0.5231	1.1782	0.0885	0.3744

3.4 Validation tests

Free decay tests are conducted first for the in-line, cross-flow, and yaw motion of the platform to validate the mooring line setup in the numerical simulation. As the mooring line configurations for θ = 0° and 90° are distinct with respect to the direction of the flow velocity, free decay tests are performed separately for the two cases. In terms of θ = 180°, the mooring line configuration mirrors that of θ = 0° and thus their results are identical. In order to obtain the decay time series in the in-line and cross-flow directions, an initial velocity of 0.05 m/s is imposed in the corresponding direction, and the platform is constrained to move in that direction only. Similarly, in the yaw free decay test, an initial angular momentum of 2 kg·m²/s is applied to the platform about the z axis, and the platform is restricted to rotate freely in the yaw direction. The fast Fourier transform (FFT) is applied to the time series to acquire the power spectral density (PSD) of the responses. Figure 5 presents the decay time series and their corresponding PSD plots in each DOF at different θ values, and the natural frequencies are compared with the experimental data in Ref. [26] denoted by the green dash dot lines in the figure. A quantitative comparison between the numerical results and the experimental data is tabulated in Table 6. It can be seen that the percentage differences in the in-line and

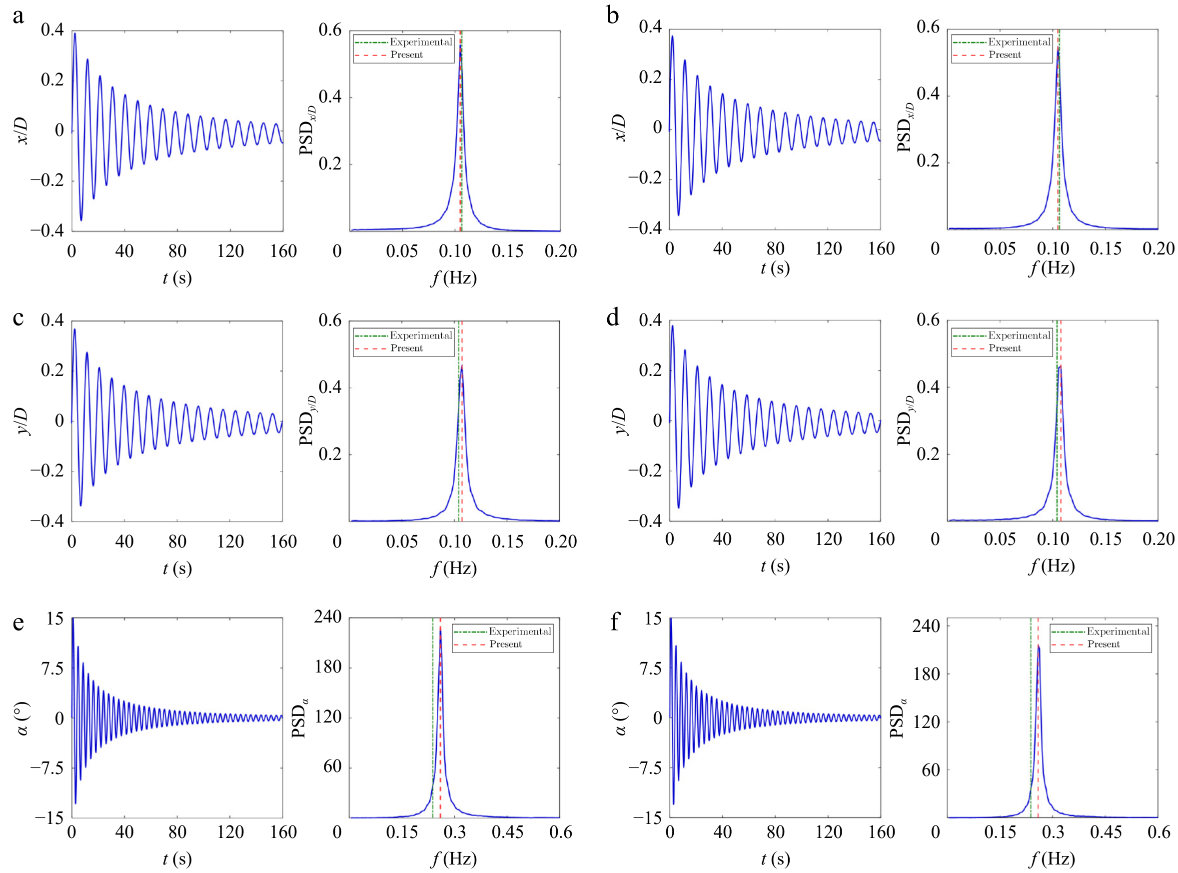

Figure 5 Decay time series and PSD plots. (a) In-line free decay for θ = 0° and 180°. (b) In-line free decay for θ = 90°. (c) Transverse free decay for θ = 0° and 180°. (d) Transverse free decay for θ = 90°. (e) Yaw free decay for θ = 0° and 180°. (f) Yaw free decay for θ = 90°.

Table 6 Comparison of the free decay test results with the experimental data

Natural frequency (Hz)	Experimental	Present	Error (%)
f_{nx} (0° and 180°)	0.1064	0.1049	1.4179
f_{ny} (0° and 180°)	0.1042	0.1074	3.1315
$f_{n\alpha}$ (0° and 180°)	0.2381	0.2598	9.1337
f_{nx} (90°)	0.1064	0.1055	0.8324
f_{ny} (90°)	0.1031	0.1069	3.6945
$f_{n\alpha}$ (90°)	0.2381	0.2600	9.1987

transverse natural frequencies (f_{nx} and f_{ny}) are below 4%, and that in the yaw natural frequency ($f_{n\alpha}$) does not exceed 10%. It is inferred that the slightly larger difference in $f_{n\alpha}$ between the experimental measurement and the numerical simulation might be attributed to the configuration of the springs and the associated nonlinearity. These discrepancies indicate that the mooring line setup in the present simulation is able to derive quite accurate inherent properties of the system.

In addition to the free decay tests, the amplitude responses computed by the numerical model are also validated against the results of the towing tank tests by Gonçalves et al. [26] for the VIM of the DeepCWind semi-submersible platform at θ = 0°. As shown in Fig. 6, the general trends of the numerical results are in good agreement with their counterparts in the experiment. A_x/D values in the present simulation and the experiment both reach their first peaks at V_R = 8 and then fluctuate around 0.05 and 0.08, respectively. There exists a notable discrepancy in A_x/D which can be attributed to the small magnitude of the in-line oscillations with random vibration components involved in it. The cross-flow response is rather significant. The maximum A_y/D also appears around V_R = 8 in both the present simulation and the preceding experiment with smaller difference in the peak A_y/D than the results of Liu et al. [25] using the RANS approach. After the peak, A_y/D decreases with increasing V_R. The variation trend of A_α with V_R in this study is highly consistent with the experimental data except for some slight deviations at the high end of V_R. Overall, the comparisons with the model test results demonstrate that the present numerical model can predict the VIM of the FOWT semi-submersible platform with acceptable accuracy.

4 Results and discussion

4.1 Amplitude responses

The variations of A_x/D, A_y/D, and A_α of the platform with V_R are illustrated in Fig. 7. As depicted in Fig. 7a, A_x/D of the DeepCWind

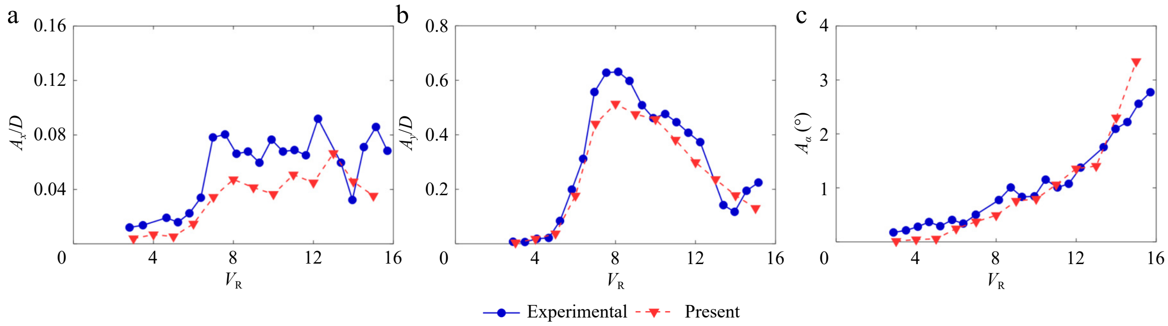

Figure 6 Comparison of the VIM response amplitudes at $\theta = 0°$ with the experimental data by Gonçalves et al. [26]. (a) In-line amplitude. (b) Cross-flow amplitude. (c) Yaw amplitude.

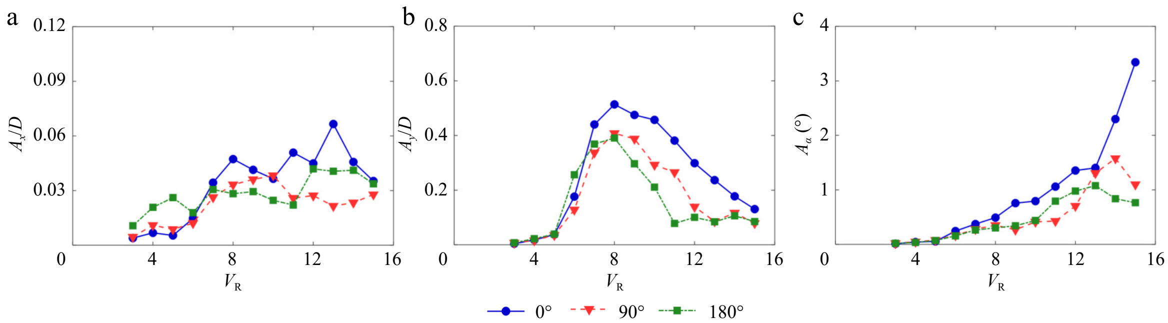

Figure 7 Variations of the VIM response amplitudes with V_R for different θ values. (a) In-line amplitude. (b) Cross-flow amplitude. (c) Yaw amplitude.

semi-submersible platform is not prominent for all the three θ values considered with the maximum A_x/D smaller than 0.08. Within the low V_R range of 3–6, a larger A_x/D is observed for θ = 180°, and that of θ = 0° is the smallest, which are consistent with the in-line amplitude response in the same V_R interval as reported by Liu et al. [27]. A_x/D at θ = 0° is larger than those of the other two θ values over the V_R range of 7–15, reaching its maximum value of approximately 0.075 at V_R = 13. In general, A_x/D exhibits a modulatory increase with the increase in V_R, and multiple local peaks appear around V_R = 8 and 11. It starts to decrease gradually when V_R exceeds 13.

As for the A_y/D curves in Fig. 7b, it is observed that the peak A_y/D values are attained at V_R = 8 for all the θ values considered. The three curves nearly coincide with each other when V_R = 3–5 and increase sharply in the V_R range of 6–8 before peaking at V_R = 8. The maximum A_y/D reaches 0.52 for θ = 0° which is evidently larger than the other two θ values. After the peak, A_y/D of θ = 0° decreases monotonically as V_R is increased from 9 to 15. The trends of the A_y/D curves of θ = 90° and 180° are similar to that of θ = 0° with a narrower lock-in range as θ is increased and they stabilise around 0.1D at V_R = 13 and 11, respectively. Such discrepancies in the transverse amplitude responses of different θ values can be possibly attributed to the different vortex interactions between the columns of the platform, which will be analysed in Section 4.5. Compared with the numerical results in the VIM studies of a simplified DeepCWind platform by Liu et al. [25] and Liu et al. [27], their peak amplitudes are significantly larger than those in the present study and the original experiment. Despite the influence of the turbulence models, this difference may be attributed to the effects of the pontoons and the cross braces. According to Gonçalves et al. [18], Liu et al. [13], and Liu et al. [42], the pontoons and cross braces interfere with the well-established wake of the columns, thereby exerting a damping effect on the VIM.

In terms of the yaw motion illustrated in Fig. 7c, the curves exhibit overall increasing trends with V_R for the θ values considered, albeit some differences at the high end of V_R. Specifically, α at θ = 0° is relatively large with a noticeable increase in the growth rate after V_R = 13. As for θ = 90° and 180°, the α curves reach their peaks at V_R = 14 and 13, respectively, with a slight decrease afterwards. The maximum α of approximately 3.5° appears at V_R = 15 and θ = 0° in the present study. Compared to the peak α of 5° in the model tests with simplified base pontoons [43] in a similar range of V_R, the peak α in this study is smaller. In addition, the present α response is also smaller than that of a deep-draft semi-submersible platform with base pontoons at θ = 45° [15], which is similar to the 0° incidence scenario in our simulation with one column in the front, two in the middle, and another one in the rear. In contrast, α in the present study is larger than its counterpart at θ = 0° in Gonçalves et al. [15] with two columns arranged in the front and the other two in the rear. Therefore, it is deduced that the yaw response is related to the presence of the pontoons and the arrangement of the columns at different θ values. In the cases where the vortex shedding of the rear columns is affected by the wake of the front ones, there exists a suppressing effect on the vortex-induced yaw motion.

4.2 Frequency responses

To clearly determine the VIM frequencies of the platform, the PSD of the response data is evaluated using the Lomb–Scargle periodogram algorithm for the unevenly distributed samples. For each DOF, the VIM frequency is normalised with the corresponding natural frequency listed in Table 6 for the different θ values.

The lock-in phenomenon takes place when the dominant response frequencies of the platform approach its natural frequencies. As shown in Figs. 8 and 9, the synchronisation is evident in the vicinity of the nondimensional frequency f_i/f_n ($i = x$, y, α, C_D, and C_L; with C_D and C_L being the fluctuating drag and lift

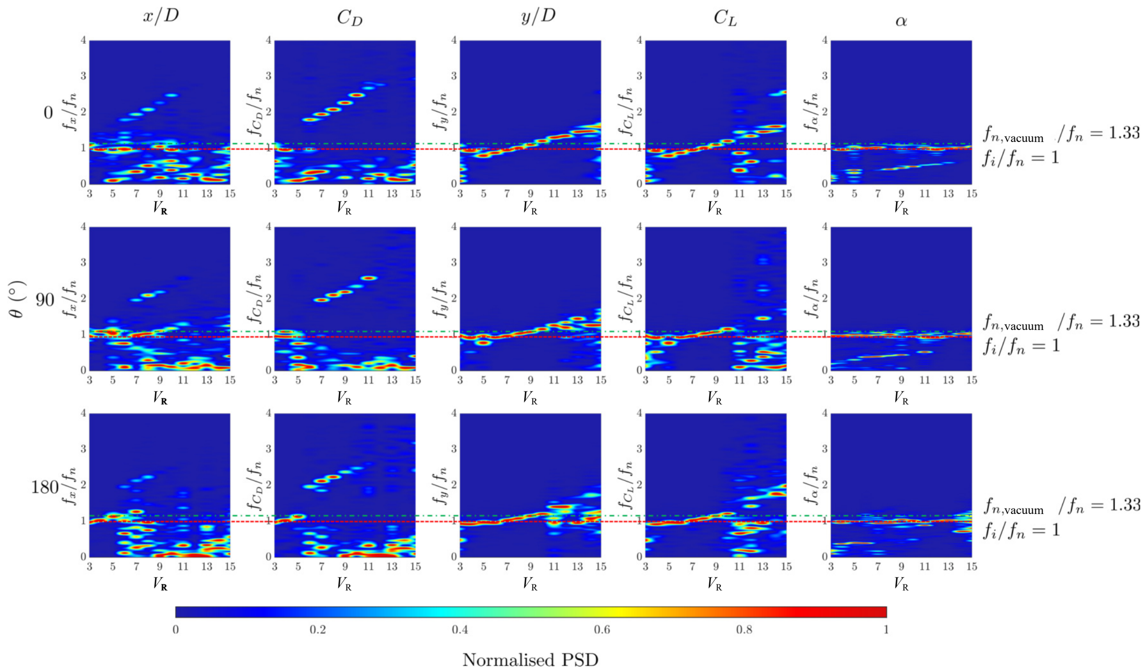

Figure 8 Normalised PSD plots of the motion responses and hydrodynamic force coefficients for different V_R and θ values.

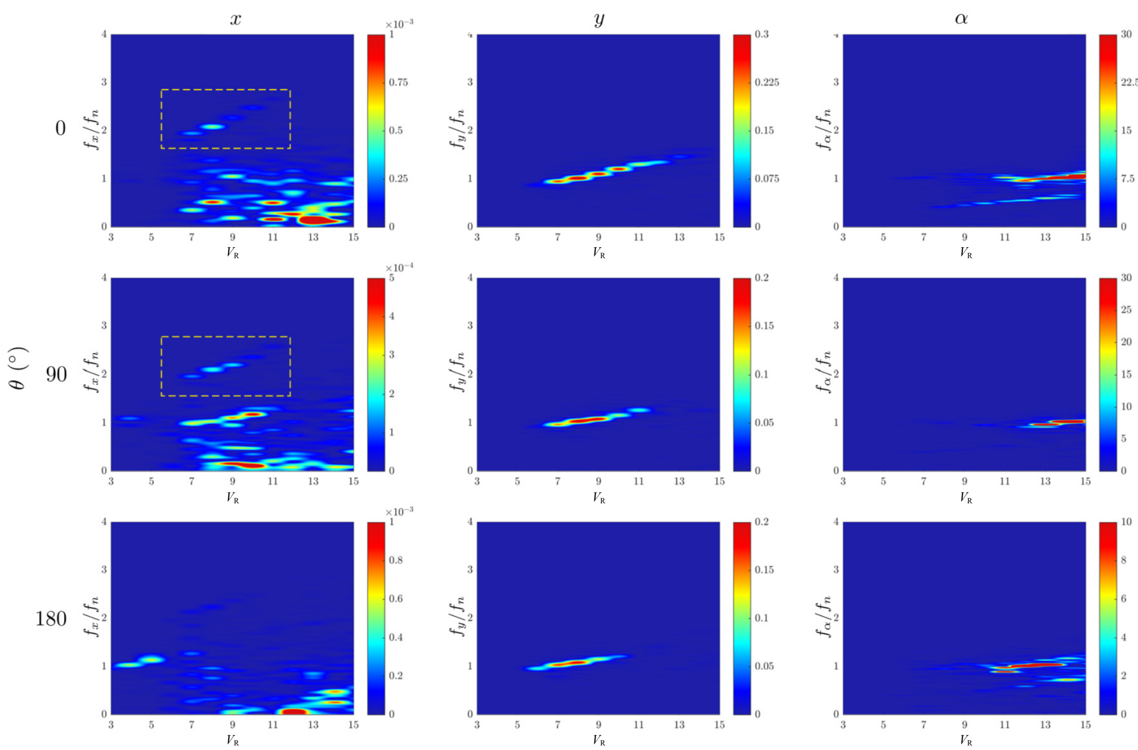

Figure 9 PSD plots of the VIM response for different V_R and θ values.

coefficients, respectively) around unity. For the different θ values, the V_R range corresponding to the lock in of the transverse response is V_R = 6–10, where the large-amplitude motion is observed as depicted in Fig. 7b. Williamson et al. [44] defined the lock-in phenomenon as the match of the excitation force frequency and the oscillation frequency of the structure. It can be seen from Fig. 8 that within the aforementioned lock-in range, the dominant frequency of C_L coincides with the dominant frequency of y, which further confirms the occurrence of lock in. At higher V_R, the lock-in phenomenon gradually becomes less pronounced accompanied by a decrease in A_y/D.

According to Khalak et al. [45] and Govardhan et al. [46], the VIV response of a circular cylinder with a low mass-damping parameter can be divided into three different branches, i.e., the initial, upper, and lower branches. Similarly, the cross-flow VIM response of the DeepCWind semi-submersible platform also exhibits analogous transitions among the three branches. For the transverse frequency response in Fig. 8, the transition from the initial branch to the upper branch is observed at V_R = 5, in accordance with $f_y/f_n \approx 1$. This observation aligns with the conclusions of Williamson et al. [44] for the 2DOF VIV of an elastically mounted circular cylinder. When V_R is increased, f_y approaches the natural frequency in vacuum ($f_y/f_n = f_{n,\text{vacuum}}/f_n$ = 1.33) at V_R = 9. As also discussed in Williamson et al. [44], from this V_R, the response transitions from the upper branch to the lower branch. Afterwards, the frequency response stabilises within the lower branch and f_y/f_n for all the three θ values remains around 1.3 in the range of V_R > 11. In Fig. 8, it is also worth noting that multiple response frequencies exist especially in the in-line motion, which are indications of the various vortex shedding frequencies from the structural members with different sizes.

It is found that the lock-in range at θ = 0° is larger than those at θ = 90° and 180°. As depicted in Fig. 9, for the cross-flow motion, the region with the prominent energy distribution of θ = 0° is much wider than the other two θ values. Compared to the results of Liu et al. [27], the lock-in range in the present research is narrower. This difference can be attributed to the influence of the pontoons and the cross braces. Within the lock-in range of the transverse motion, higher harmonic frequency components are witnessed in the in-line response as encompassed by the yellow boxes in Fig. 9. The normalised PSD plots reveal a slight overlap between the dominant frequencies of C_D and x. Moreover, the dominant frequency of C_D is twice that of C_L. These characteristics indicate that the in-line motion, to some extent, is affected by the alternately shed vortices. Nevertheless, the inertia force has stronger influence on the in-line motion.

In terms of the yaw response, it can be seen from Fig. 8 that the dominant frequency close to the natural frequency of the yaw motion is evident at low V_R, but the overall frequency distribution is relatively scattered. f_α varies around f_α/f_n = 1 when V_R > 11 at θ = 0° and 90° and when V_R > 7 at θ = 180°. Its low frequency components are not as strong as the in-line response. Recalling the results in Fig. 7c, A_α remains around its peak within the V_R range of 12–15 for θ = 90° and within the V_R range of 11–15 for θ = 180°. It is observed from Fig. 9 that the energy of the yaw motion is also mainly concentrated in the V_R range of 11–15 for θ = 0° and 180° and in the V_R range of 13–15 for θ = 90°, respectively. Similar to the cross-flow motion, it can be inferred that these V_R ranges are lock-in ranges for the vortex-induced yaw motion. The results also indicate that the vortex-induced yaw motion is affected by multiple factors, such as the natural frequency in the yaw degree of freedom and the variations in the vortex shedding modes between the different columns [47].

4.3 Hydrodynamic coefficients

The variations of $\bar{C}_D$ and C'_D with V_R are illustrated in Figs. 10a and 10b. As shown in the figure, both $\bar{C}_D$ and C'_D at θ = 0° are larger than the other two θ values. Similar to the θ = 90° case, $\bar{C}_D$ and C'_D of θ = 0° reach their respective peaks at V_R = 8. However, for θ = 180°, the peak $\bar{C}_D$ appears at V_R = 7, and it is 10% larger than that for θ = 90°. When θ = 180°, $\bar{C}_D$ attains larger values at low V_R of 3 and 4, corresponding to the larger A_x/D in Fig. 7a. This observation was also reported in the model tests of Gonçalves et al. [26]. The bell shape curves of $\bar{C}_D$ and C'_D with respect to V_R are consistent with the variation trends of the A_y/D curves in Fig. 7b. According to Govardhan et al. [48], when the transverse response reaches its maximum, it possesses a coupling effect with the streamwise hydrodynamic force. Similar phenomenon was also confirmed by Liu et al. [27] and Tian et al. [49] in their numerical studies on the VIM of three-column semi-submersible platforms.

Similar to the A_y/D curves in Fig. 7b, C'_L under the different θ values in Fig. 10c increases rapidly with V_R, reaching its peak at V_R around 6 and 7. After the peak, it starts to decrease as V_R is further increased. The peak of C'_L for θ = 180° also takes place earlier than the other two θ values. C'_L of the different θ values becomes steady from V_R = 10. The same trend has also been reported by Li et al. [50] and Liu et al. [27] for the various types of semi-submersible platforms, and the plateau of C'_L can be explained by the interaction

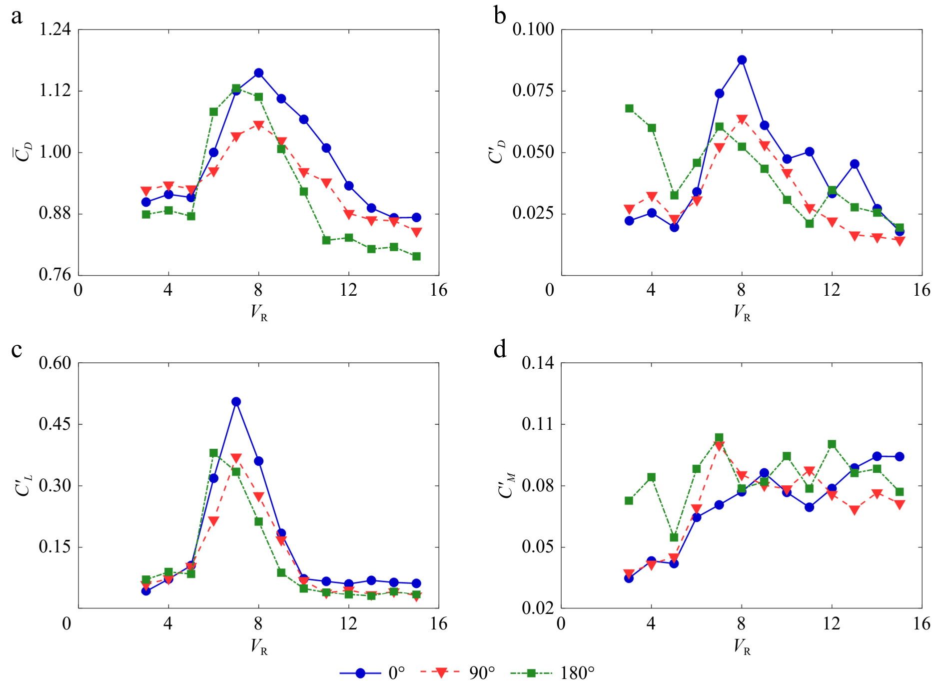

Figure 10 Variations of the drag, lift and moment coefficients with V_R for different θ values. (a) $\bar{C}_D$, (b) C'_D, (c) C'_L, and (d) C'_M.

between the two hydrodynamic force components, namely the added mass force and the excitation force as suggested by Govardhan et al. [46].

The variations of the rms value of the yawing moment coefficient (C'_M) in Fig. 10d show that C'_M increases with increasing V_R when $V_R < 6$ and stabilises around 0.1 in the higher V_R range. Overall, C'_M demonstrates significantly modulatory characteristics with multiple peaks. Based on the detailed analyses of the hydrodynamic forces acting on each column of the multi-column semi-submersible platforms [50,51], the vortex-induced yaw motion is believed to be mainly related to the frequencies of the forces acting on each column and the axis about which the resultant moment is determined. That is the possible reason why it is not necessary for A_α to vary consistently with C'_M. Considering the A_α curves in Fig. 7c, C'_M for all the three θ values remains at relatively high levels with the increase in α at high V_R. C'_M for $\theta = 0°$ is found to be larger than the other two θ values, which may contribute to the more significant yaw response in the corresponding V_R range.

$F_x(t)$ and $F_y(t)$ can be decomposed into the forces in phase with the corresponding accelerations (the added mass forces) and the forces in phase with the corresponding velocities (the excitation forces) as

$$F_x(t) = -\rho V C_{ax}\ddot{x}(t) + \frac{\rho A_p U^2}{2\sqrt{2}\dot{x}_{\mathrm{rms}}} C_{ex}\dot{x}(t) \tag{18}$$

$$F_y(t) = -\rho V C_{ay}\ddot{y}(t) + \frac{\rho A_p U^2}{2\sqrt{2}\dot{y}_{\mathrm{rms}}} C_{ey}\dot{y}(t) \tag{19}$$

where V is the volume of the displaced water. Following Xu et al. [52] and Wang et al. [53], a least squares method is adopted to determine the added mass and excitation coefficients.

$$C_{ax} = \frac{1}{\rho V}\frac{S_1 S_5 - S_2 S_3}{S_2^2 - S_1 S_4} \tag{20}$$

$$C_{ex} = \frac{2\sqrt{2}\dot{x}_{\mathrm{rms}}}{\rho A_p U^2}\frac{S_2 S_5 - S_3 S_4}{S_2^2 - S_1 S_4} \tag{21}$$

$$C_{ay} = \frac{1}{\rho V}\frac{S_6 S_{10} - S_7 S_8}{S_7^2 - S_6 S_9} \tag{22}$$

$$C_{ey} = \frac{2\sqrt{2}\dot{y}_{\mathrm{rms}}}{\rho A_p U^2}\frac{S_7 S_{10} - S_8 S_9}{S_7^2 - S_6 S_9} \tag{23}$$

where $S_1 = \sum_{i=1}^{N_s}[\dot{x}(t_i)]^2$, $S_2 = \sum_{i=1}^{N_s}[\dot{x}(t_i)\ddot{x}(t_i)]$, $S_3 = \sum_{i=1}^{N_s}[\dot{x}(t_i)F_x(t_i)]$, $S_4 = \sum_{i=1}^{N_s}[\ddot{x}(t_i)]^2$, $S_5 = \sum_{i=1}^{N_s}[\ddot{x}(t_i)F_x(t_i)]$, $S_6 = \sum_{i=1}^{N_s}[\dot{y}(t_i)]^2$, $S_7 = \sum_{i=1}^{N_s}[\dot{y}(t_i)\ddot{y}(t_i)]$, $S_8 = \sum_{i=1}^{N_s}[\dot{y}(t_i)F_y(t_i)]$, $S_9 = \sum_{i=1}^{N_s}[\ddot{y}(t_i)]^2$, $S_{10} = \sum_{i=1}^{N_s}[\ddot{y}(t_i)F_y(t_i)]$, and N_s is the total number of samples.

Figures 11a and 11b depict the variations of the in-line and cross-flow added mass coefficients (C_{ax} and C_{ay}) with V_R. C_{ax} for all the three θ values decreases sharply to zero when $V_R < 5$ and crosses zero at V_R around 5 and 6. After reaching zero, it decreases to about −0.6 at V_R around 8 which coincides with the peak $\bar{C}_D$ and C'_D as shown in Figs. 10a and 10b. With a further increase in V_R, C_{ax} reaches a plateau indicating the attenuation of the effect of the inertia force. C_{ay} also shows a decreasing trend with the increase in V_R and crosses zero at $V_R = 10$ for all the three θ values considered in the present study. It is mentioned by Modarres-Sadeghi [54] that the larger C_{ay} in the range of V_R = 6–8 manifests the synchronisation with the vortex shedding frequency, and this V_R range matches the lock-in range of the transverse response. As suggested by Jauvtis et al. [55], for the 2DOF VIV of a circular cylinder, the zero-crossing point of C_{ax} is associated with the beginning of the lock-in range while the zero-crossing point of C_{ay} marks the end of the synchronisation between the response frequency and the vortex shedding frequency. The same conclusions can also be reached based on the present results for the VIM of the DeepCWind semi-submersible platform.

The in-line and cross-flow excitation coefficients (C_{ex} and C_{ey}) in Figs. 11c and 11d define the energy transfer between the fluid and the structure [53,56]. Bringing the added mass and the excitation forces to the left-hand side of the translational motion equations.

$$(m_x + \rho V C_{ax})\ddot{x}(t) + \left(c_x - \frac{\rho A_p U^2}{2\sqrt{2}\dot{x}_{rms}} C_{ex}\right)\dot{x}(t) + k_x x(t) = 0 \tag{24}$$

$$(m_y + \rho V C_{ay})\ddot{y}(t) + \left(c_y - \frac{\rho A_p U^2}{2\sqrt{2}\dot{y}_{rms}} C_{ey}\right)\dot{y}(t) + k_y y(t) = 0 \tag{25}$$

It can be interpreted from Eqs. (24) and (25) that positive C_{ex} and C_{ey} lead to negative flow-induced damping, and the energy is transferred from the fluid to the structure. Whereas negative C_{ex} and C_{ey} result in positive flow-induced damping which dissipates the kinetic energy of the structure. Due to the complex structure of the DeepCWind semi-submersible platform, intricate wake–structure interactions, such as the impingement of the vortices and the reattachment of the shear layers on the structural members of the platform are ubiquitous. Therefore, it is expected that C_{ex} and C_{ey} vary significantly with V_R, especially in the lock-in region. At high V_R, C_{ex}, and C_{ey} gradually approach zero signifying the weakening influence of the vortices on the platform. When V_R = 6–10, C_{ey} values of $\theta = 0°$ and 180° are positive suggesting that the energy is transferred from the fluid to the platform. In contrast, C_{ey} of $\theta = 90°$ is negative which is an indication of the dissipation of the energy through flow-induced damping. These findings are also reflected by the orbital orientations of the motion trajectories to be discussed in Section 4.4.

4.4 Motion trajectories

Figure 12 shows the motion trajectories of the platform in the *xy* plane for different θ and V_R values and the trajectory lines are coloured by α. The arrows in the figure represent the orbital directions of the trajectories with the red arrows standing for the counterclockwise trajectories and the blue ones being the clockwise trajectories. It can be found from the figure that the trajectories are irregular in the non-lock-in regions because of the low frequency components in the in-line motion. The trajectories for $V_R < 6$ demonstrate no clear patterns due to the small-amplitude in-line and cross-flow VIM. As V_R is increased, the transverse response becomes more pronounced, and the trajectories in the lock-in range exhibit nonrepeatable figure-eight shapes which are the evidence of the occurrence of dual resonance [57]. When V_R exceeds 11, the trajectories become disordered, which can be attributed to the irregular wake patterns at high V_R, leading to the strong variations in the phase difference between the in-line and cross-flow responses [58].

Within the lock-in range, the trajectories are more regular compared to those in the non-lock-in regions. Oblique figure-eight shape trajectories are observed for θ = 0° and 180°, while the motion trajectories of the platform at θ = 90° display raindrop shapes. As discussed by Dahl et al. [59] in their study on the VIV of a circular cylinder, the shapes of the trajectories are closely related

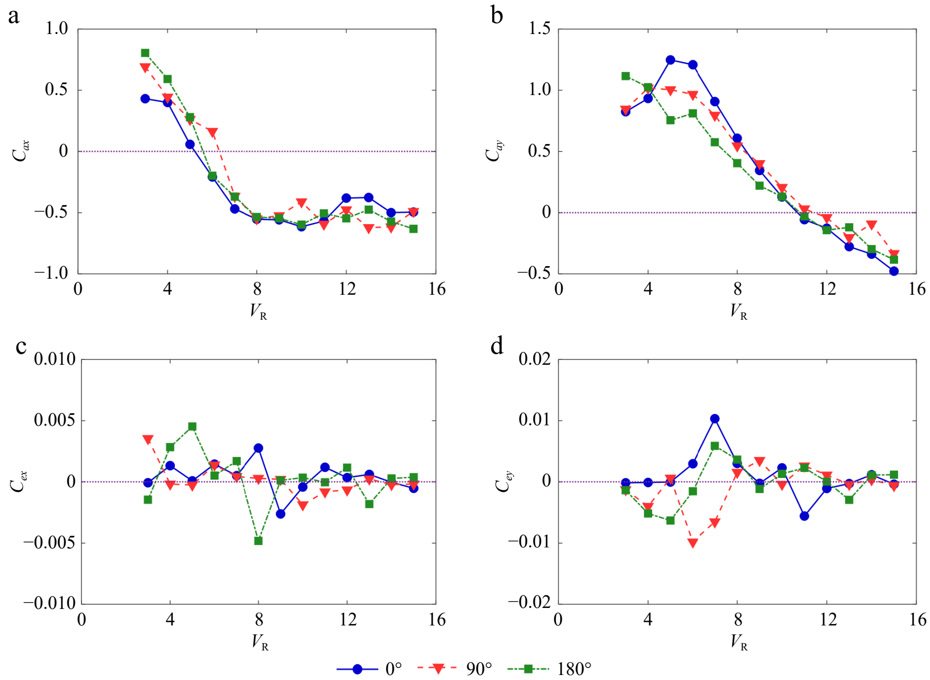

Figure 11 Variations of the added mass and excitation coefficients with V_R for different θ values. (a) C_{ax}, (b) C_{ay}, (c) C_{ex}, and (d) C_{ey}.

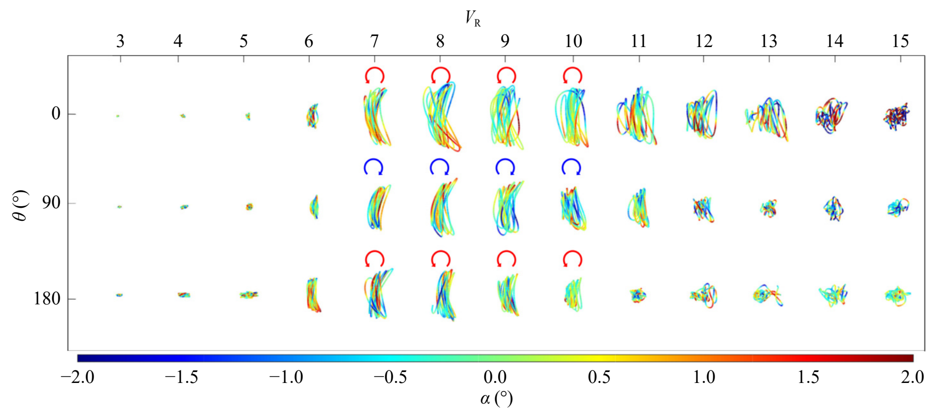

Figure 12 Motion trajectories for different V_R and θ values. Red arrows represent counterclockwise trajectories, and blue arrows represent clockwise trajectories.

to the oscillation frequencies in the streamwise and the transverse directions. The Lissajous figures with oblique figure-eight shapes and raindrop shapes suggest that there is a frequency component in the in-line motion that is identical to the dominant frequency of the cross-flow motion [58,60], which is also confirmed by the results in Fig. 8. In term of the orbital orientations of the trajectories in the lock-in range, the trajectories for θ = 0° and 180° are in the counterclockwise direction. While for θ = 90°, the trajectories of the platform are clockwise. According to Dahl et al. [59] and Bourguet et al. [61], the upstream motion in a counterclockwise trajectory leads to a closer proximity of the structure and the recently shed vortices. Hence, the energy is transferred from the fluid to the body. Whereas in clockwise orbits, the flow acts as the damping of the VIM. Therefore, in Fig. 12, the counterclockwise trajectories are indications of energy being transferred from the ambient fluid to the DeepCWind platform, and the clockwise trajectories signify that the energy is dissipated via hydrodynamic damping. These findings agree with the analyses of C_{ex} and C_{ey} in Section 4.3. In addition, similar conclusions have also been reported in Ref. [62] for the VIM of a spar-type FOWT platform.

4.5 Wake patterns

Investigating the influence of the complex vortex fields on the VIM characteristics of the semi-submersible FOWT platform is of paramount importance for unveiling the FSI mechanisms. This section presents the two-dimensional (2D) and 3D vortex structures for different θ values at V_R = 5, 8, and 15. These three V_R values correspond to the three different VIM response branches.

Figure 13 shows the nondimensional spanwise vorticity ($\omega^* = \omega_z D/U$, where ω_z is the dimensional spanwise vorticity) contours on two xy planes at V_R = 5. The vertical coordinates of the two cross sections are located at the COG of the platform (z = 0) and the centres of the base columns ($z = d_{BC}$), respectively. The contours are arranged in the sequence of the time instants a–e in the half cycle of the transverse VIM. At this particular V_R, it is known from the previous discussion that the response amplitudes are relatively small. For z = 0, the shear layers detached from the surfaces of the side columns extend to some extent before breaking up. When θ = 0°, the shear layers of the upstream side column reattach onto the MC suppressing its vortex shedding and making the wake relatively chaotic. The inner shear layers of the two downstream side columns

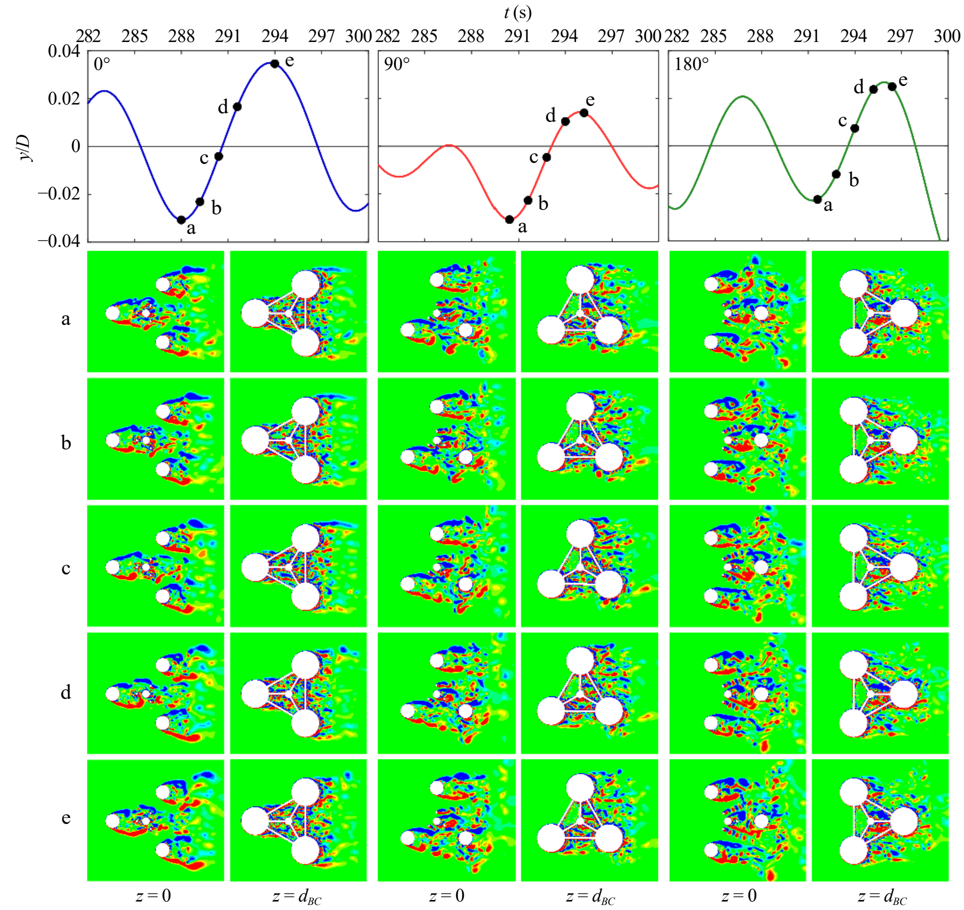

Figure 13 Contours of ω^* at five different time instants on two cross sections (vertical coordinate of platform COG: $z = 0$ and vertical coordinate of base column centres: $z = d_{BC}$) for different θ values and $V_R = 5$.

are affected by the combined wake. At $\theta = 90°$, the vortices from the upstream side column only interact with the lower shear layer of the MC, and alternately shed vortices are observed for the MC. The wake of the top side column is less affected with a clear vortex street formed. In contrast, the downstream side column is immersed in the combined wake of the upstream side column and the MC whose vortex shedding is greatly interfered by the upstream wake. As for $\theta = 180°$, in terms of the upstream side columns, their vortex shedding is relatively independent with almost negligible interactions with the vortices shed from the upstream cross braces. Subject to the vortex shedding of the MC, two inclined vortex streets with two single vortices shed per cycle (2S) wake modes are observed for the upstream cross braces. In the meanwhile, the downstream cross brace is completely immersed in the wake of the MC, and its vortex shedding is suppressed. The detached vortices from the MC impinge on the surfaces of the downstream side column, and the wake is essentially a combined wake from the two structural members.

For $z = d_{BC}$, the larger sizes of the side base columns delay the separations of the boundary layers. According to the research of Liu et al. [24] on the VIV of a cylindrical structure with a base column, the base column can significantly alter the flow fields, leading to an extension of the lock-in range even in the presence of the free end effects. The presence of the base column increases the viscous damping which inhibits the VIM. Given the large diameter of the base columns, the small gaps between two base columns and the influence of the pontoons make the large vortices break into smaller ones, and the vortices are only witnessed behind each base column. In the cases of $\theta = 90°$ and 180°, the vorticity in the areas enclosed by the delta pontoons and the Y pontoons are not very strong, which suppress the generation of vortices in these areas.

The vortex shedding at eight time instants a–h within one cycle of the transverse motion at $V_R = 8$ in the lock-in range is presented in Fig. 14. For the three θ values considered in the present study, the vortices behind the side columns exhibit an alternating shedding pattern, which leads to a significant increase in the lift force and contributes to the large response amplitudes at this very V_R. On the $z = 0$ cross section, for $\theta = 0°$, the large-amplitude VIM of the platform offers enough space for the free shear layers of the upstream side column to roll up into vortices instead of reattaching onto the MC. The impingement of the vortices on the MC and the cross braces suppresses the vortex shedding from these structural members. As for the downstream side columns, their vortex shedding is uninfluenced. In terms of $\theta = 90°$, when the platform is at its bottom extreme (time instants a and h), the vortices from the upstream side column interact with the MC and the cross braces. Whereas, they switch to interacting with the downstream side column as the platform moves towards its top extreme (time instants d and e). A fully developed vortex street is found behind the top side column. When $\theta = 180°$, independent vortex shedding is observed behind the two upstream side columns. The vortices detached from the MC produce a convective effect on the downstream side column and disturb its shear layers, resulting in an irregular wake behind it. Under such perturbations, the vortices in the wake of the downstream side column cannot get fully

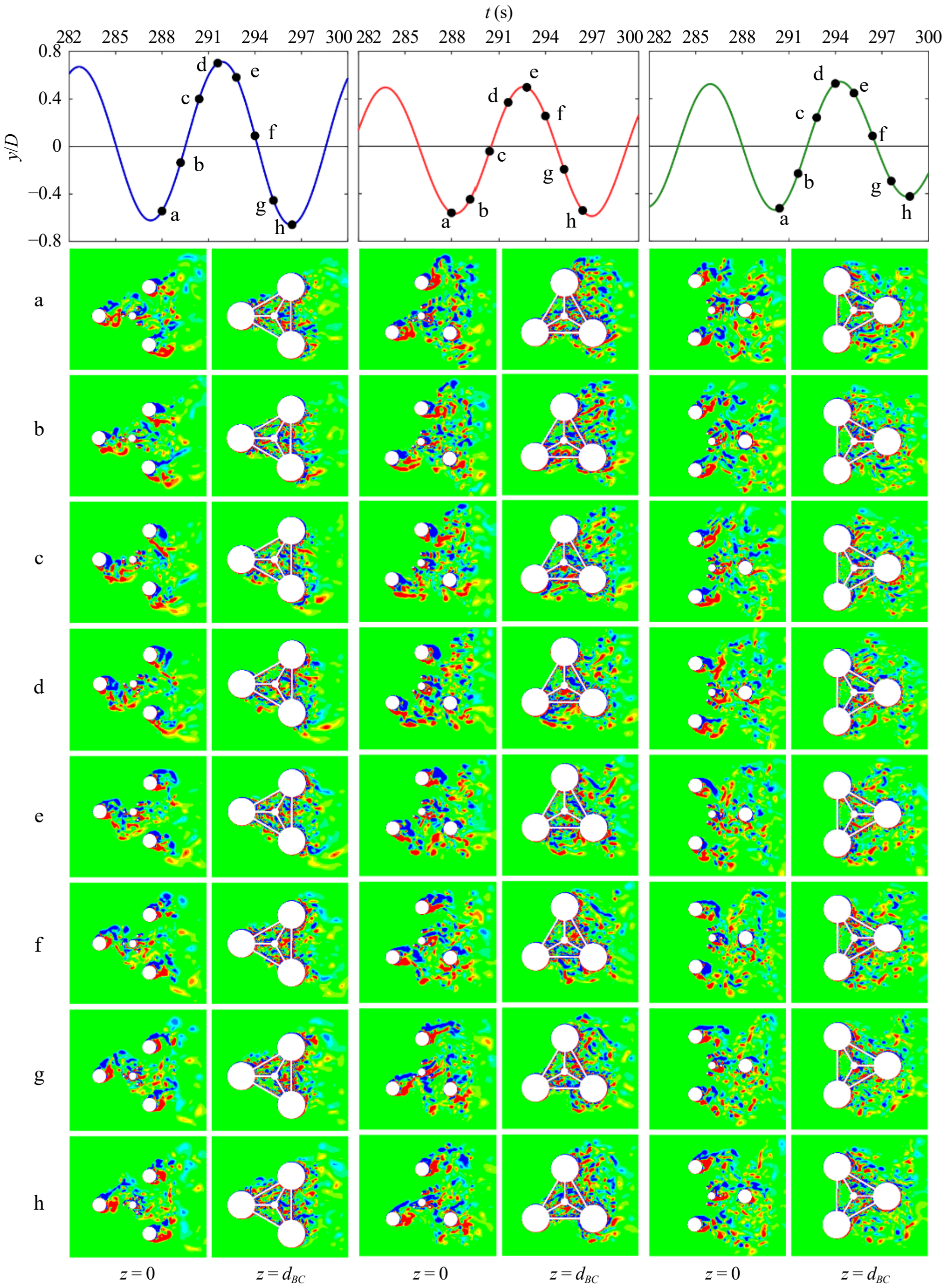

Figure 14 Contours of ω^* at eight different time instants on two cross sections (vertical coordinate of platform COG: z = 0 and vertical coordinate of base column centres: $z = d_{BC}$) for different θ values and V_R = 8.

developed, and the correlation of the lift force is reduced. Similar vortex fields have also been reported by Tian et al. [49] for the VIM of a three-column platform. Based on their conclusions, the downstream column being influenced by the upstream vortices is likely to be the reason for the smaller response amplitudes.

On the lower cross section of $z = d_{BC}$, it can be seen that the vortices shed from the upstream base columns are obstructed by the pontoons. Additionally, under the three θ values considered, evident shear layer reattachment is observed for the areas enclosed by the pontoons due to the small distances between the structural members, and the vortices are strongly affected by the base columns with a larger diameter. Outside the central area, vortices are formed on the side surfaces of the upstream base column. However, the two co-rotating vortex pairs formed per cycle (2C) vortex shedding mode described by Liu et al. [24] does not appear. The possible reason for the absence of the 2C wake pattern can be the suppression effect of the pontoons on the vortex shedding, which prevents the formation of the vortex pairs.

The instantaneous 3D vortex structures around the platform at V_R = 8 for different θ values are visualised in Fig. 15. The left column of the figure provides the isometric views of the platform with the detailed vortex structures while the right column of the figure shows their counterparts viewed from the bottom. The 3D vortex structures are described by the iso-surfaces of $\lambda_2 = -3$, where λ_2 is the second eigenvalue of the symmetric tensor $\boldsymbol{S}^2 + \boldsymbol{\Omega}^2$ [63], where $\boldsymbol{S}$ and $\boldsymbol{\Omega}$ are the symmetric and antisymmetric parts, respectively. the velocity gradient tensor $\nabla \boldsymbol{u}$. The iso-surfaces are coloured by the normalised streamwise velocity (u/U), where u is the local velocity in the streamwise direction. Complex flow fields of the DeepCWind platform undergoing the VIM at high Re are

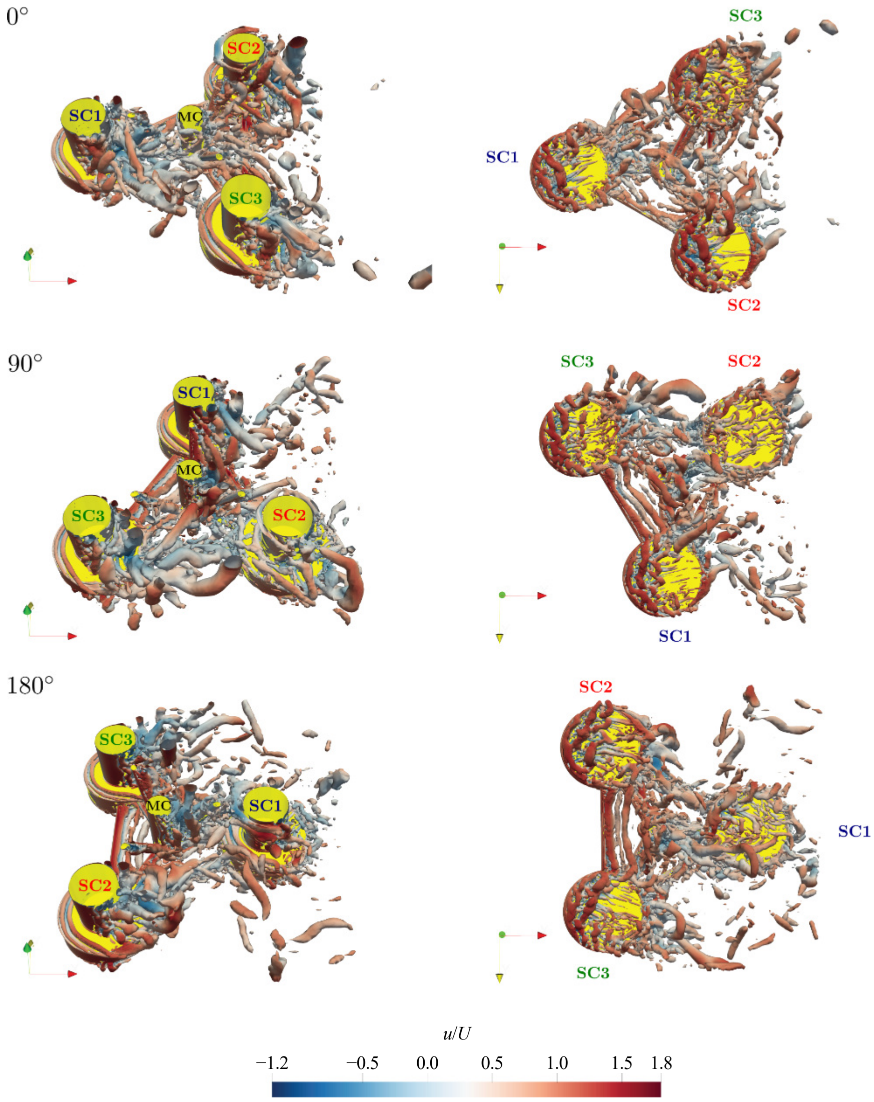

Figure 15 Instantaneous 3D vortex structures for different θ values at $V_R = 8$.

observed. For the three θ values considered, a pair of shear layers is generated from the upstream columns and quickly breaks down to form turbulent vortices. For the side column 1 (SC1) at $\theta = 0°$, the side column 3 (SC3) at $\theta = 90°$ and the side columns 2 and 3 (SC2 and SC3) at $\theta = 180°$, the vortices generated from the side surfaces of the base columns gradually coalesce with those generated from the surfaces of the upper columns to form the dominant vortices acting on the surfaces of the downstream columns. Subsequently, the vortex shedding from the downstream columns is affected, leading to the asynchronous vortex shedding from the different columns. This asynchronous vortex shedding is more pronounced when $\theta = 90°$ and 180° resulting in the smaller peak A_y/D values compared to the case of $\theta = 0°$.

Further examining the vortex fields in Fig. 15, it can be seen that a pair of vortex tubes forms from the top edges of the upstream base columns and is ultimately attracted into the trailing vortices from the upper columns becoming part of the dominant vortices. In addition, parallel vortex tubes are formed behind the upstream delta lower pontoons and fragmented by the MC, the Y lower pontoons, and the cross braces. This disturbs the vortex fields around the MC and to some degree and inhibits the VIM responses. Relatively obvious vortices are generated at the bottom edges of the base columns and then react on the bottom of the base columns, which verifies the existence of the free end effects [24] in the present study.

In Fig. 16, the contours of ω^* at four time instants a–d within one cycle of the yaw motion on $z = 0$ and $z = d_{BC}$ when $V_R = 15$ are displayed. At this V_R, the flow separation is further delayed with the separation points moving downstream, which causes elongated shear layers on the side columns as well as the MC. This wake pattern leads to the downstream side column being shielded by the upstream vortex flow. The hydrodynamic forces on the downstream side column are consequently affected. It can be observed from the time histories of α that the vortex-induced yaw motion of $\theta = 0°$ is stronger with the wake exhibiting a more pronounced 2S mode. As for the cases of $\theta = 90°$ and 180°, the vortex fields are similar to those at $V_R = 5$. The synchronisation of the vortex shedding from the downstream side columns is worse than the $\theta = 0°$ scenario, which appears to have some suppression effects on the yaw motion.

When $\theta = 180°$ at $V_R = 15$, 2S vortex shedding modes are observed in the wake of the cross braces, and two vortex streets are symmetrically located on the two sides of the MC as depicted in the red boxes in Fig. 16. It is deduced that this symmetric wake pattern

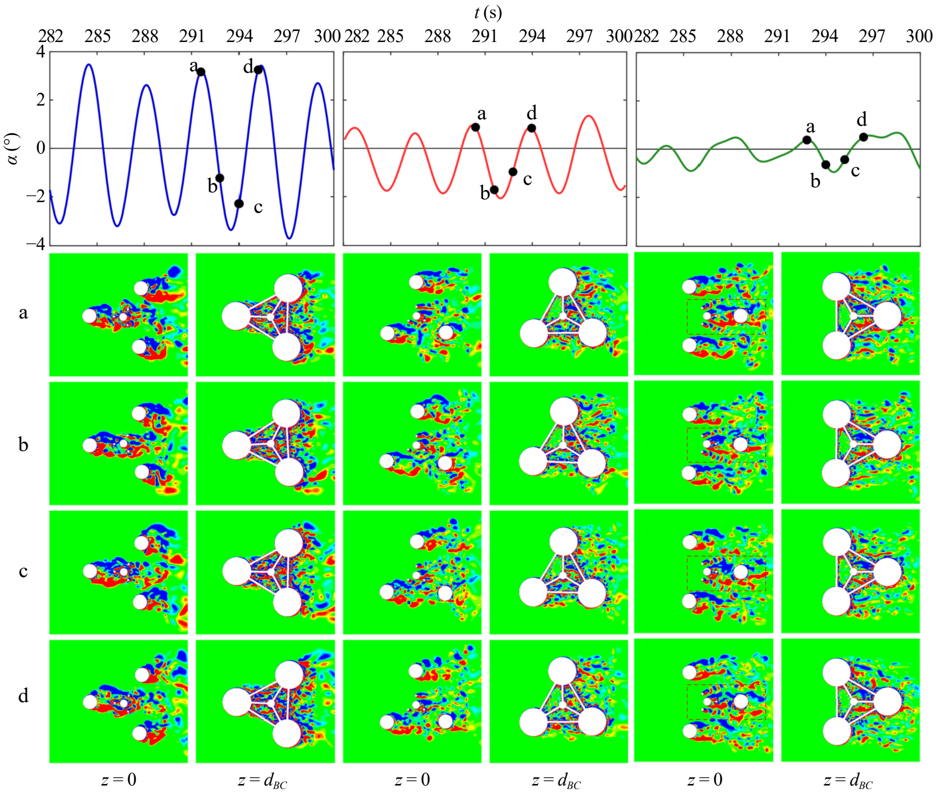

Figure 16 Contours of ω^* at four different time instants on two cross sections (vertical coordinate of platform COG: $z = 0$ and vertical coordinate of base column centres: $z = d_{BC}$) for different θ values and $V_R = 15$.

generates an additional restoring moment and thus attenuates the yaw motion of the platform. This feature is not obvious at $V_R = 5$ and 8. For $V_R = 5$, the vortices shed from the cross braces are influenced by the shear layers of the MC, making the symmetric pattern more prone to be disturbed. Furthermore, at $V_R = 8$, the two cross braces demonstrate completely asymmetric vortex shedding.

The 3D vortex structures in the central part of the platform at $V_R = 15$ are presented in Fig. 17. As shown in the figure, when $\theta = 180°$, the vortices are formed and shed in the rear of the symmetrical cross braces. The overall vortex field in the central part appears to be more symmetric than the $\theta = 0°$ and 90° cases, and the resulting forces tend to maintain the balance, generating a restoring moment against the yaw motion. In contrast, for $\theta = 0°$, the vortex field is strongly affected by the upstream vortices. The convective impacts at the centre of the platform lead to the formation of counter-rotating vortices depending on α and thus sustain the yaw motion.

5 Conclusion

In this study, the VIM responses of the OC4 DeepCWind semi-submersible FOWT platform are investigated numerically. A high-fidelity FSI simulation tool based on the open source CFD framework OpenFOAM is developed and utilised with LES being employed to simulate the turbulent flow. The scale of the model is 1:72.72. Three θ values, i.e., $\theta = 0°$, 90°, and 180° are examined, and V_R ranges from 3 to 15. The numerical results are validated against the published experimental data and further analysed to explore the effect of θ on the VIM characteristics of the DeepCWind platform. The main conclusions of the present research are summarised as follows:

A_y/D of the platform is relatively large with the lock-in phenomenon occurring in the V_R range of 6–10. The maximum A_y/D of 0.52 is observed for $\theta = 0°$ at $V_R = 8$. When $\theta = 90°$ and 180°, the interference between the upstream vortices and the vortices from the side columns affects the overall synchronisation of the vortex shedding from the different columns, which results in a decrease in the lift force and a reduction in the VIM response.

The lock in of the yaw motion takes place at high V_R. When $\theta = 180°$ and $V_R \geq 13$, two symmetric vortex streets are generated from the cross braces of the platform, thereby producing a restoring moment that inhibits the yaw motion. Moreover, for $\theta = 180°$, the vortex field in the central part of the platform is less influenced by the upstream vortices. The combined action of these mechanisms contributes to the smaller A_α in $\theta = 180°$ case at the high end of V_R.

Both C_{ax} and C_{ay} decrease with increasing V_R and the zero-crossing points of C_{ax} and C_{ay} correspond to the start and the end of the lock-in range, respectively. C_{ey} values of $\theta = 0°$ and 180° are positive while that of $\theta = 90°$ is negative, indicating the differences in the directions of the energy transfer between the fluid and the structure. Figure-eight shape and raindrop shape motion trajectories are observed for the platform when it is subject to the VIM. The trajectories are mostly counterclockwise for $\theta = 0°$ and 180°, whereas clockwise trajectories are more common when $\theta = 90°$. The pontoons and cross braces narrow the gap between the columns, impeding the development of the large-scale vortices.

In general, the present numerical results are in good agreement with the existing experimental data and provide insights into the response characteristics and FSI mechanisms of the VIM of the DeepCwind semi-submersible FOWT platform. Nevertheless, similar to the previous CFD studies on the VIM of the offshore platforms, the influence of the free surface is not taken into account.

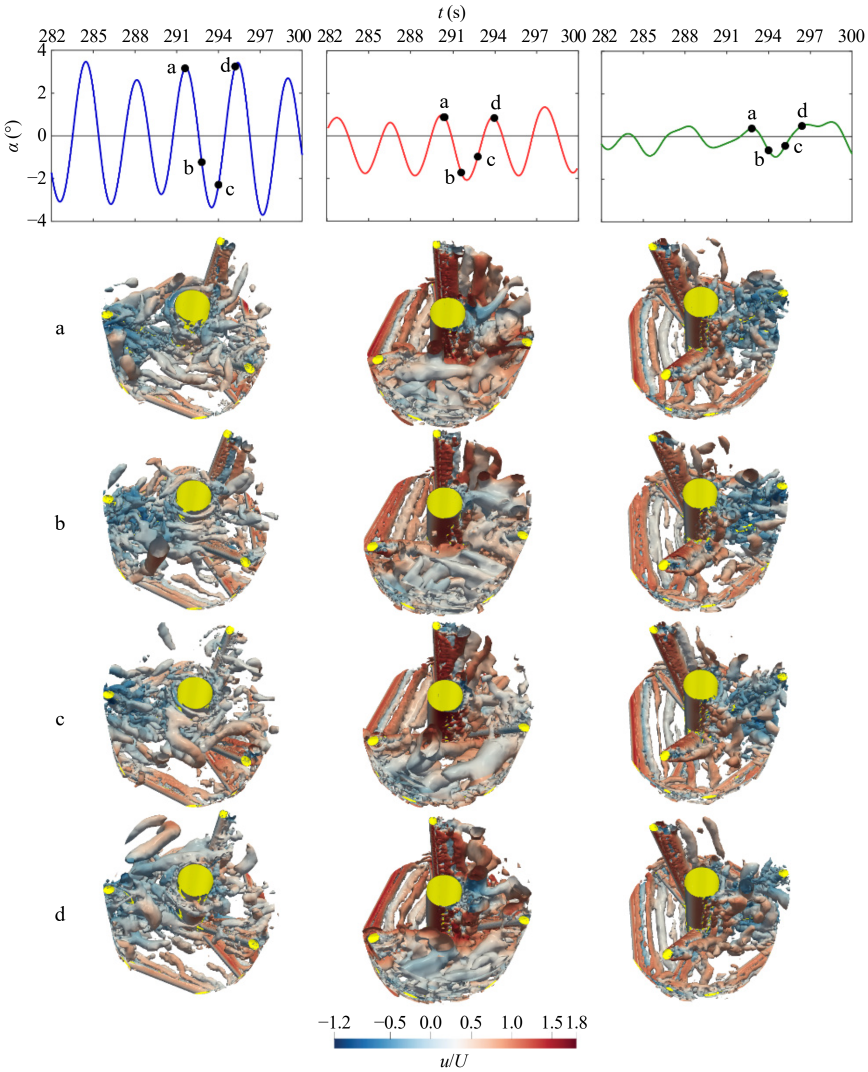

Figure 17 3D vortex structures at four different time instants in one cycle of yaw motion for different θ values at $V_R = 15$.

Moreover, the effect of the aerodynamic loads is not considered in both the model tests and the current simulation. More systematic investigations addressing these issues will be performed in the future research.

Acknowledgements

None.

Author contribution statement

Xianghan Yin is responsible for investigation, formal analysis, validation, visualization, writing—original draft. Enhao Wang is responsible for conceptualization, methodology, supervision, funding acquisition, writing—review & editing. Hongteng Xu is responsible for data curation, visualization. Hao Wu is responsible for data curation, writing—review & editing. Yuanchuan Liu is responsible for methodology, writing—review & editing. Binbin Li is responsible for supervision and writing—review & editing. Lin Lin is responsible for writing—review & editing. Qing Xiao is responsible for writing—review & editing. Atilla Incecik is responsible for writing—review & editing. All the authors have approved the final manuscript.

Data availability

The data that support the findings of this study are available from the corresponding author upon reasonable request.

Declaration of competing interest

All the contributing authors report no conflicts of interest in this work.

Funding

This work is granted by the National Natural Science Foundation of China (Grant Nos. 52271282 and 51909189), Guangdong Basic and Applied Basic Research Foundation (Grant No. 2024A1515240018), and Shenzhen Science and Technology Programme (Grant Nos. RCYX20231211090210018 and WDZC20231125203917001).

Use of AI statement

None.

References

[1] International Energy Agency. (2022). Renewables 2022: Analysis and Forecasts to 2027. Paris: International Energy Agency.

[2] Vargas, S. A., Esteves, G. R. T., Maçaira, P. M., Bastos, B. Q., Cyrino Oliveira, F. L., Souza, R. C. (2019). Wind power generation: A review and a research agenda. *J. Clean. Prod* 218, 850–870.

[3] Karimirad, M. (2014). Offshore Energy Structures: For Wind Power, Wave Energy and Hybrid Marine Platforms. Cham: Springer.

[4] Subbulakshmi, A., Verma, M., Keerthana, M., Sasmal, S., Harikrishna, P., Kapuria, S. (2022). Recent advances in experimental and numerical methods for dynamic analysis of floating offshore wind turbines—An integrated review. *Renew. Sustain. Energy Rev* 164, 112525.

[5] Liu, Y. C., Li, S. W., Yi, Q., Chen, D. Y. (2016). Developments in semi-submersible floating foundations supporting wind turbines: A comprehensive review. *Renew. Sustain. Energy Rev* 60, 433–449.

[6] Tian, Z., Liu, F. S., Zhou, L., Yuan, C. F. (2020). Fluid–structure interaction analysis of offshore structures based on separation of transferred responses. *Ocean Eng* 195, 106598.

[7] Papi, F., Bianchini, A. (2022). Technical challenges in floating offshore wind turbine upscaling: A critical analysis based on the NREL 5 MW and IEA 15 MW Reference Turbines. *Renew. Sustain. Energy Rev* 162, 112489.

[8] Waals, O. J., Phadke, A. C., Bultema, S. (2007). Flow induced motions on multi column floaters. In Proceedings of the ASME 2007 26th International Conference on Offshore Mechanics and Arctic Engineering, San Diego, USA.

[9] Rijken, O., Leverette, S. (2008). Experimental study into vortex induced motion response of semi submersibles with square columns. In Proceedings of the ASME 2008 27th International Conference on Offshore Mechanics and Arctic Engineering, Estoril, Portugal.

[10] Fujarra, A. L. C., Rosetti, G. F., de Wilde, J., Gonçalves, R. T. (2012). State-of-the-art on vortex-induced motion: A comprehensive survey after more than one decade of experimental investigation. In Proceedings of the ASME 2012 31st International Conference on Ocean, Offshore and Arctic Engineering, Rio de Janeiro, Brazil.

[11] Yin, D., Passano, E., Jiang, F. J., Lie, H., Wu, J., Ye, N., Sævik, S., Leira, B. J. (2022). State-of-the-art review of vortex-induced motions of floating offshore wind turbine structures. *J. Mar. Sci. Eng* 10, 1021.

[12] Hussain, A., Nah, E., Fu, R., Gupta, A. (2009). Motion comparison between a conventional deep draft semi-submersible and a dry tree semi-submersible. In Proceedings of the ASME 2009 28th International Conference on Ocean, Offshore and Arctic Engineering, Honolulu, USA.

[13] Liu, M. Y., Xiao, L. F., Lu, H. N., Xiao, X. L. (2017). Experimental study on vortex-induced motions of a semi-submersible with square columns and pontoons at different draft conditions and current incidences. *Int. J. Nav. Arch. Ocean Eng* 9, 326–338.

[14] Gonçalves, R. T., Fujarra, A. L. C., Rosetti, G. F., Kogishi, A. M., Koop, A. (2015). Effects of column designs on the VIM response of deep-draft semi-submersible platforms. In Proceedings of the Twenty-fifth (2015) International Ocean and Polar Engineering Conference, Kona, USA. https://onepetro.org/ISOPEIOPEC/proceedings-abstract/ISOPE15/All-ISOPE15/15047

[15] Gonçalves, R. T., Fujarra, A. L. C., Rosetti, G. F., Kogishi, A. M., Koop, A. (2018). Experimental study of the column shape and the roughness effects on the vortex-induced motions of deep-draft semi-submersible platforms. *Ocean Eng* 149, 127–141.

[16] Gonçalves, R. T., Chame, M. E. F., Hannes, N. H., de Paula Lopes, P. P. S., Hirabayashi, S., Suzuki, H. (2020). FIM—Flow-induced motion of three-column platforms. *Int. J. Offshore Polar Eng* 30, 177–185.

[17] Liu, M. Y., Xiao, L. F., Lu, H. N., Shi, J. Q. (2016). Experimental investigation into the influences of pontoon and column configuration on vortex-induced motions of deep-draft semi-submersibles. *Ocean Eng* 123, 262–277.

[18] Gonçalves, R. T., Suzuki, H., Cenci, F., Fujarra, A. L. C., Hirabayashi, S. (2019). Experimental study of the effect of the pontoon presence on the flow-induced motion of a semi-submersible platform with four square columns. In Proceedings of the ASME 2019 38th International Conference on Ocean, Offshore and Arctic Engineering, Glasgow, UK.

[19] Rijken, O., Leverette, S. (2009). Field measurements of vortex induced motions of a deep draft semisubmersible. In Proceedings of the ASME 2009 28th International Conference on Ocean, Offshore and Arctic Engineering. Honolulu, USA.

[20] Wu, G. Y., Ma, W., Kramer, M., Kim, J. W., Jang, H., O'Sullivan, J. (2014). Vortex-induced motions of a column-stabilized floater Part II: CFD benchmark and prediction. In Proceedings of the Deep Offshore Technology International Conference, Aberdeen, UK. https://www.researchgate.net/publication/281240545_Vortex_Induced_Motions_of_a_Column_Stabilized_Floater_Part_II_CFD_Benchmark_and_Prediction

[21] Tran, T. T., Kim, D. H. (2016). Fully coupled aero-hydrodynamic analysis of a semi-submersible FOWT using a dynamic fluid body interaction approach. *Renew. Energy* 92, 244–261.

[22] Huang, Y., Zhuang, Y., Wan, D. C. (2021). Hydrodynamic study and performance analysis of the OC4-DeepCWind platform by CFD method. *Int. J. Comput. Methods* 18, 2050020.

[23] Zhou, Y., Xiao, Q., Peyrard, C., Pan, G. (2021). Assessing focused wave applicability on a coupled aero-hydro-mooring FOWT system using CFD approach. *Ocean Eng* 240, 109987.

[24] Liu, Y. C., Liu, F. S., Wang, E. H., Xiao, Q., Li, L. (2020). The effect of base column on vortex-induced vibration of a circular cylinder with low aspect ratio. *Ocean Eng* 196, 106822.

[25] Liu, Y. C., Wang, T., Liu, F. S. (2020). Numerical investigation of vortex-induced motion of a semi-submersible floating offshore wind turbine. In Proceedings of the 30th International Ocean and Polar Engineering Conference, Online. https://onepetro.org/ISOPEIOPEC/proceedings-abstract/ISOPE20/All-ISOPE20/446688

[26] Gonçalves, R. T., Chame, M. E. F., Silva, L. S. P., Koop, A., Hirabayashi, S., Suzuki, H. (2021). Experimental flow-induced motions of a FOWT semi-submersible type (OC4 Phase II Floater). *J. Offshore Mech. Arct. Eng* 143, 012004.

[27] Liu, Y. C., Ge, D. J., Bai, X. L., Li, L. (2023). A CFD study of vortex-induced motions of a semi-submersible floating offshore wind turbine. *Energies*. 16, 698.

[28] Tian, C. L., Xiao, L. F., Liu, M. Y., Yang, L. J., Liu, J. (2019). Numerical study on vortex-induced motions of semisubmersibles with three columns with different sections types. In Proceedings of the ASME 2019 38th International Conference on Ocean, Offshore and Arctic Engineering, Glasgow, UK.

[29] Gonçalves, R. T., Hannes, N. H., Chame, M. E. F., Lopes, P. P. S. P., Hirabayashi, S., Suzuki, H. (2020). FIM—Flow-induced motions of four-column platforms. *Appl. Ocean Res* 95, 102019.

[30] Zhao, W. W., Wei, Z. Y., Wan, D. C. (2022). Numerical investigation on the effects of current headings on vortex induced motions of a semi-submersible. *J. Hydrodyn* 34, 382–394.

[31] Kim, S. J., Spernjak, D., Holmes, S., Vinayan, V., Antony, A. (2015). Vortex-induced motion of floating structures: CFD sensitivity considerations of turbulence model and mesh refinement. In Proceedings of the ASME 2015 34th International Conference on Ocean, Offshore and Arctic Engineering, St. John's, Canada.

[32] Huang, K., Chen, H. C., Chen, C. R. (2010). Vertical riser VIV simulation in uniform current. *J. Offshore Mech. Arct. Eng* 132, 031101.

[33] Huang, K., Chen, H. C., Chen, C. R. (2011). Numerical scheme for riser motion calculation during 3-D VIV simulation. *J. Fluids Struct* 27, 947–961.

[34] Wang, E. H., Xiao, Q. (2016). Numerical simulation of vortex-induced vibration of a vertical riser in uniform and linearly sheared currents. *Ocean Eng* 121, 492–515.

[35] Chen, C. R., Chen, H. C. (2016). Simulation of vortex-induced motions of a deep draft semi-submersible in current. *Ocean Eng* 118, 107–116.
[36] Robertson, A., Jonkman, J., Masciola, M., Song, H., Goupee, A., Coulling, A., Luan, C. (2014). Definition of the Semisubmersible Floating System for Phase II of OC4. Golden: National Renewable Energy Laboratory.
[37] Nicoud, F., Ducros, F. (1999). Subgrid-scale stress modelling based on the square of the velocity gradient tensor. *Flow Turbul. Combust* 62, 183–200.
[38] Stein, E., de Borst, R., Hughes, T. J. R. (2004). Encyclopedia of Computational Mechanics. Chichester: John Wiley.
[39] Issa, R. I. (1986). Solution of the implicitly discretised fluid flow equations by operator-splitting. *J. Comput. Phys* 62, 40–65.
[40] Newmark, N. M. (1959). A method of computation for structural dynamics. *J. Eng. Mech* 85, 67–94.
[41] Rentschler, M., Chandramouli, P., Vaz, G., Viré, A., Gonçalves, R. T. (2023). CFD code comparison, verification and validation for decay tests of a FOWT semi-submersible floater. *J. Ocean Eng. Mar. Energy* 9, 233–254.
[42] Liu, M. Y., Xiao, L. F., Liang, Y. B., Tao, L. B. (2017). Experimental and numerical studies of the pontoon effect on vortex-induced motions of deep-draft semi-submersibles. *J. Fluids Struct* 72, 59–79.
[43] Gonçalves, R. T., Chame, M. E. F., Hannes, N. H., de Paula Lopes, P. P. S., Hirabayashi, S., Suzuki, H. (2018). Experimental study on flow-induced motion of an array of three cylinders with circular, square, and diamond sections. In Proceedings of the 28th International Ocean and Polar Engineering Conference, Sapporo, Japan. https://onepetro.org/ISOPEIOPEC/proceedings-abstract/ISOPE18/All-ISOPE18/20325
[44] Williamson, C. H. K., Govardhan, R. (2004). Vortex-induced vibrations. *Annu. Rev. Fluid Mech* 36, 413–455.
[45] Khalak, A., Williamson, C. H. K. (1999). Motions, forces and mode transitions in vortex-induced vibrations at low mass-damping. *J. Fluids Struct* 13, 813–851.
[46] Govardhan, R., Williamson, C. H. K. (2000). Modes of vortex formation and frequency response of a freely vibrating cylinder. *J. Fluid Mech* 420, 85–130.
[47] Liang, Y. B., Tao, L. B. (2017). Interaction of vortex shedding processes on flow over a deep-draft semi-submersible. *Ocean Eng* 141, 427–449.
[48] Govardhan, R., Williamson, C. H. K. (2002). Resonance forever: Existence of a critical mass and an infinite regime of resonance in vortex-induced vibration. *J. Fluid Mech* 473, 147–166.
[49] Tian, C. L., Liu, M. Y., Xiao, L. F., Lu, H. N., Wang, J. (2021). Numerical studies on flow-induced motions of a semi-submersible with three circular columns. *Int. J. Nav. Arch. Ocean Eng* 13, 599–616.
[50] Li, S. M., Zhao, W. W., Wan, D. C. (2018). The hysteresis phenomenon between force and motion in vortex-induced motion of semi-submersible platform. In Proceedings of the 13th OpenFOAM Workshop, Shanghai, China. https://d.wanfangdata.com.cn/conference/WFHYXW646396
[51] Zhao, W. W., Zou, L., Wan, D. C., Hu, Z. Q. (2018). Numerical investigation of vortex-induced motions of a paired-column semi-submersible in currents. *Ocean Eng* 164, 272–283.
[52] Xu, W. H., Wu, H. K., Jia, K., Wang, E. H. (2021). Numerical investigation into the effect of spacing on the flow-induced vibrations of two tandem circular cylinders at subcritical Reynolds numbers. *Ocean Eng* 236, 109521.
[53] Wang, E. H., Zhao, S. H., Xu, W. H., Xiao, Q., Li, B. (2023). Effect of splitter plate length on FIV of circular cylinder. *Int. J. Mech. Sci* 254, 108413.
[54] Modarres-Sadeghi, Y. (2022). Introduction to Fluid–Structure Interactions. Cham: Springer.
[55] Jauvtis, N., Williamson, C. H. K. (2004). The effect of two degrees of freedom on vortex-induced vibration at low mass and damping. *J. Fluid Mech* 509, 23–62.
[56] Yin, D. C., Lie, H., Baarholm, R. J. (2017). Prototype Reynolds number VIV tests on a full-scale rigid riser. In Proceedings of the ASME 2017 36th International Conference on Ocean, Offshore and Arctic Engineering, Trondheim, Norway.
[57] Dahl, J. M., Hover, F. S., Triantafyllou, M. S., Oakley, O. H. (2010). Dual resonance in vortex-induced vibrations at subcritical and supercritical Reynolds numbers. *J. Fluid Mech* 643, 395–424.
[58] Wang, E. H., Xiao, Q., Incecik, A. (2017). Three-dimensional numerical simulation of two-degree-of-freedom VIV of a circular cylinder with varying natural frequency ratios at Re = 500. *J Fluids Struct* 73, 162–182.
[59] Dahl, J. M., Hover, F. S., Triantafyllou, M., Dong, S., Karniadakis, G. E. (2007). Resonant vibrations of bluff bodies cause multivortex shedding and high frequency forces. *Phys. Rev. Lett* 99, 144503.
[60] Kang, Z., Jia, L. S. (2013). An experiment study of a cylinder's two degree of freedom VIV trajectories. *Ocean Eng* 70, 129–140.
[61] Bourguet, R., Karniadakis, G. E., Triantafyllou, M. S. (2013). Phasing mechanisms between the in-line and cross-flow vortex-induced vibrations of a long tensioned beam in shear flow. *Comput. Struct* 122, 155–163.
[62] Carlson, D. W., Modarres-Sadeghi, Y. (2018). Vortex-induced vibration of spar platforms for floating offshore wind turbines. *Wind Energy* 21, 1169–1176.
[63] Jeong, J., Hussain, F. (1995). On the identification of a vortex. *J. Fluid Mech* 285, 69–94.